Deep–Sea Research II 198 (2022) 105055

Contents lists available at ScienceDirect

Deep-Sea Research Part II

journal homepage: www.elsevier.com/locate/dsr2

Dynamically downscaled projections of ocean acidification for the Bering Sea

D.J. Pilcher [a,b,*], J.N. Cross [b], A.J. Hermann [a,b], K.A. Kearney [a,c], W. Cheng [a,b], J.T. Mathis [d]

[a] Joint Institute for the Study of the Atmosphere and Ocean, University of Washington, Seattle, WA, USA
[b] NOAA Pacific Marine Environmental Laboratory, Seattle, WA, USA
[c] NOAA Alaska Fisheries Science Center, Seattle, WA, USA
[d] Georgetown University, School of Foreign Service, Washington, D.C, USA

ARTICLE INFO

Keywords:
Bering sea
Dynamical downscaling
Regional modeling
Ocean acidification

ABSTRACT

A regional ocean biogeochemical model for the Bering Sea is used to dynamically downscale three Earth System Models from the CMIP5 archive under the RCP 8.5 and RCP 4.5 scenarios. These continuous model runs, completed in conjunction with the Alaska Climate Integrated Modeling Project (ACLIM), span the 2006–2100 timeframe and project continued warming, freshening, and ocean acidification (OA) for the Bering Sea shelf region over the 21st Century, with larger magnitude changes in the RCP 8.5 scenario. The downscaled projections suggest that annual average surface seawater aragonite saturation state (Ω_{arag}) for the Bering Sea shelf will decrease by 0.63–0.86 under RCP 8.5 and 0.18–0.43 under RCP 4.5 by 2100. Surface pH values decrease by 0.31–0.35 under RCP 8.5 and 0.07–0.13 under RCP 4.5. Seasonally, $\Omega_{arag} < 1$ conditions start to emerge for ~2 months per year during winter between 2015 and 2030 under both climate change scenarios. Under RCP 8.5, the duration of these undersaturated conditions grows to ~5 months per year by 2100, occurring from mid-October through mid-March. Under RCP 4.5, these conditions remain constrained to 2–3 months per year by 2100. In both scenarios, summer months maintain conditions of $\Omega_{arag} > 1$ due to primary productivity, though the maximum in Ω_{arag} is greatly reduced under RCP 8.5. Spatially, the regions of greatest pH and Ω_{arag} decline are the southeastern Bering Sea shelf and the outer shelf domain near the shelf break. Linear trends in carbonate variables between our downscaled simulations and the Earth System Model (ESM) output are comparable and indistinguishable compared to the model spread. However, bottom water trends differ somewhat between the ESM and our downscaled simulations, with the latter more consistently resolving the different shelf domains. The OA information provided by these downscaled simulations can help inform biological sensitivity experiments and longterm strategic planning for marine fisheries management.

1. Introduction

The global oceans absorb 25–31% of present annual anthropogenic carbon emissions, and have taken up approximately 39% of all anthropogenic fossil carbon emissions since the start of the Industrial Revolution (Khatiwala et al., 2009; McKinley et al., 2017; Gruber et al., 2019; Friedlingstein et al., 2020). However, the dissolution of CO_2 in seawater shifts the marine carbonate system to a state of lower pH and reduced carbonate saturation states in a process referred to as ocean acidification (OA; Feely et al., 2004). Experimental studies have shown that the reduced pH and carbonate saturation states may negatively impact some marine organisms, particularly marine calcifiers (Kroeker et al., 2013; Doney et al., 2020). Observational evidence suggests that global pH has already decreased by 0.1 (~30% increase in $[H^+]$) since the start of the Industrial Revolution, with global Earth System Models (ESM) projecting an additional decrease of ~0.3 (~100% increase in $[H^+]$) by 2100 under high CO_2 emissions scenarios (Orr et al., 2005; Bopp et al., 2013; Kwiatkowski et al., 2020). Arctic and subarctic oceans are particularly vulnerable to OA because these systems have naturally low pH and carbonate saturation states due to colder water temperatures that increase the solubility of CO_2 (Orr et al., 2005; Fabry et al., 2009). Furthermore, large Arctic river systems deliver substantial amounts of terrestrial carbon and freshwater to Arctic waters, which further decrease carbonate saturation states (Chierici and Fransson, 2009;

* Corresponding author. Joint Institute for the Study of the Atmosphere and Ocean, University of Washington, Seattle, WA, USA.
E-mail address: darren.pilcher@noaa.gov (D.J. Pilcher).

https://doi.org/10.1016/j.dsr2.2022.105055
Received 9 April 2021; Received in revised form 23 February 2022; Accepted 5 March 2022
Available online 13 March 2022

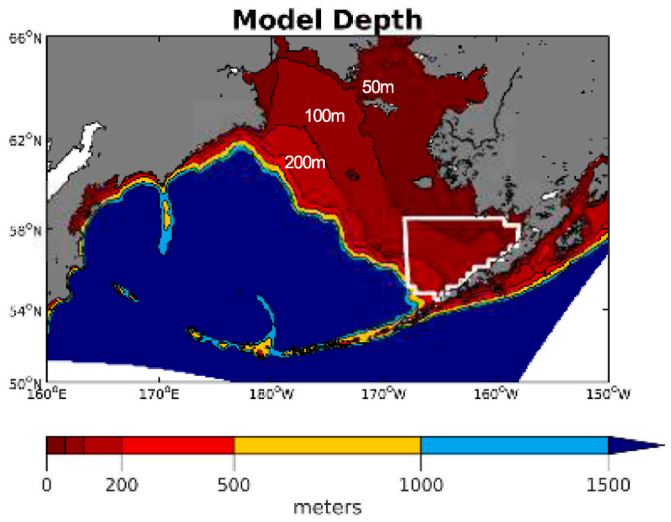

Fig. 1. Bering10K model domain with color shading for model depth. The black contour lines for the 50, 100, and 200 m isobaths are labeled, representing the boundary for the inner, middle, and outer shelf domain respectively. The white boxed area is the Eastern Bering Sea Bristol Bay red king crab management region. (For interpretation of the references to color in this figure legend, the reader is referred to the Web version of this article.)

Mathis et al., 2011; Semiletov et al., 2016). Increased precipitation, sea-ice loss, and river runoff with climate change may further strengthen these effects, though a concurrent increase in nutrient delivery may further complicate the net effect (Steiner et al., 2014; Terhaar et al., 2019, 2021a, 2021b). Small shifts in ocean dissolved inorganic carbon (DIC) concentrations can cause large swings in some carbonate variables, including pH and Ω_{arag}. In a system naturally close to important biological and geochemical thresholds, these combined effects make Alaskan waters especially susceptible to OA.

The Bering Sea system is composed of a deep offshore basin and a wide coastal shelf. The shelf is further divided into three physically distinct regions consisting of the inner, middle, and outer shelf domains, typically defined by the 50 m, 100 m, and 200 m isobaths, respectively (Askren and thesis, 1972; Coachman, 1986; Stabeno et al., 1999). Substantial portions of the inner and middle shelf are normally covered by sea ice during winter months, though the outer shelf can also be near completely ice covered during particularly cold years (Stabeno and Bell, 2019). Sea-ice retreat typically occurs in April–May, though warmer water temperatures and southerly winds have led to earlier ice retreats (February–March) and reduced sea-ice extent in recent years (Stabeno and Bell, 2019). The timing of the spring ice retreat impacts the initiation of the spring bloom; an earlier ice retreat enhances surface stratification through freshening and delays the bloom to May–June, while a later ice retreat initiates an earlier ice-associated bloom in colder water, which is associated with larger, lipid-rich diatoms (Hunt et al., 2002, 2011). This variability in bloom timing and composition can further alter benthic-pelagic energy pathways and have reverberating effects throughout the entire ecosystem (Moore and Stabeno, 2015). The complexity of this system has made it challenging to understand the physical-biological connections and make informed predictions for how the system will respond to climate change. Global models generally disagree on whether continued warming will lead to a net increase or decrease in productivity. A longer growing season with less sea-ice extent may increase productivity through the first half of the 21st Century, however increasing stratification and decreasing nutrient supply may counter this effect and lead to a net decrease by the end of the century (Bopp et al., 2013; Vancoppenolle et al., 2013). Observational studies do tend to support a recent increase in productivity (Arrigo and van Dijken, 2015; Lewis et al., 2020), though there is still considerable uncertainty, especially regarding how increased river runoff and coastal erosion may mobilize additional nutrients (Vonk et al., 2012; Terhaar et al., 2019).

Ocean waters that are already undersaturated with respect to aragonite (a polymorph of calcium carbonate) occur seasonally on the Bering Sea shelf, indicated by aragonite saturation state (Ω_{arag}) values less than one (Mathis et al., 2011). These conditions occur along the inner shelf domain and at the bottom on the middle and outer shelf domains (Mathis et al., 2011). Low Ω_{arag} on the inner shelf is driven by freshwater runoff from river systems, primarily the Yukon and Kuskokwim Rivers. This freshwater runoff is supersaturated with carbon due to respiration of terrestrial organic matter (Striegl et al., 2007). When mixed with the coastal water mass, this runoff increases the DIC to total alkalinity (TA) ratio, which pushes the marine CO_2 system towards lower pH and Ω_{arag} (Mathis et al., 2011; Pilcher et al., 2019). Low bottom water Ω_{arag} on the middle and outer shelf is driven by bacterial respiration of sinking organic matter generated by surface mixed layer phytoplankton productivity (Mathis et al., 2011). Evidence of subsurface calcium carbonate dissolution on the shelf further suggests that these seasonal manifestations of OA impacts are already occurring (Cross et al., 2013). Previous projections using a global-scale Earth System Model indicate that annual average surface Bering Sea surface waters will become undersaturated with respect to aragonite ($\Omega_{arag} < 1$) on the annual mean by around 2062 under a high CO_2 emissions scenario (Mathis et al., 2015a).

The Bering Sea is one of the most productive marine ecosystems on Earth and supports a U.S. fishery that provides $3 billion in annual value and at least 40% of total U.S. fish catch by weight (Wiese et al., 2012). The heavy reliance of many Alaskan coastal communities on these fisheries for commercial and subsistence use puts them at greater risk to the effects of OA (Mathis et al., 2015b). Experimental studies have noted that larval and juvenile red king crab (*Paralithodes camtschaticus*) and Tanner crab (*Chionoecetes bairdi*) survival are both reduced under lower pH conditions (Long et al., 2013a,b; Long et al., 2016). Based on these sensitivities to pH, a bioeconomic model predicted a substantial decline in Bristol Bay red king crab catch if the effects of OA were not considered within the fishery management process (Seung et al., 2015; Punt et al., 2016). Behavioral changes in Pacific cod (*Gadus macrocephalus*) larvae have been shown to reduce size and lipid content by 2 weeks of age, but this response was reversed (i.e. larger size and higher lipid content, though not statistically significant) by 5 weeks of age, pointing to a stage-specific response (Hurst et al., 2019). Conversely, some pelagic fish species such as walleye pollock (*Gadus chalcogrammus*) have displayed resilience to OA in experimental settings (Hurst et al., 2013). However, pelagic fish species may still be indirectly affected through food web changes. For example, pteropod shell dissolution has already been observed in the Bering Sea and pteropod populations are at high risk with continued OA (Bednaršek et al., 2021).

Earth System Models (ESMs) are one of the best available tools to project how the Earth system may respond to anthropogenic climate change. These fully coupled models provide skillful reproductions of historical ocean conditions at the basin scale, but are often less effective in regional settings, due in part to insufficient spatial resolution and the parameterization or omission of critical coastal processes (Ward et al., 2020). A growing number of efforts have utilized statistical and dynamical techniques to downscale output from an ESM to a regional setting (Hermann et al., 2019, 2021; Holdsworth et al., 2021; Siedlecki et al., 2021). Dynamical downscaling techniques require the use of a regional ocean model and are computationally expensive due to the higher spatial resolution. Despite this computational cost, the added benefit of higher spatial resolution and the capacity to resolve critical coastal shelf features makes the technique particularly appealing for providing climate change information within marine fisheries settings (Drenkard et al., 2021). Recent work by the Alaska Climate Integrated Modeling project (ACLIM) demonstrated this benefit by combining dynamically downscaled projections of ocean conditions in the Bering Sea with a variety of climate-enhanced fisheries and socio-economic

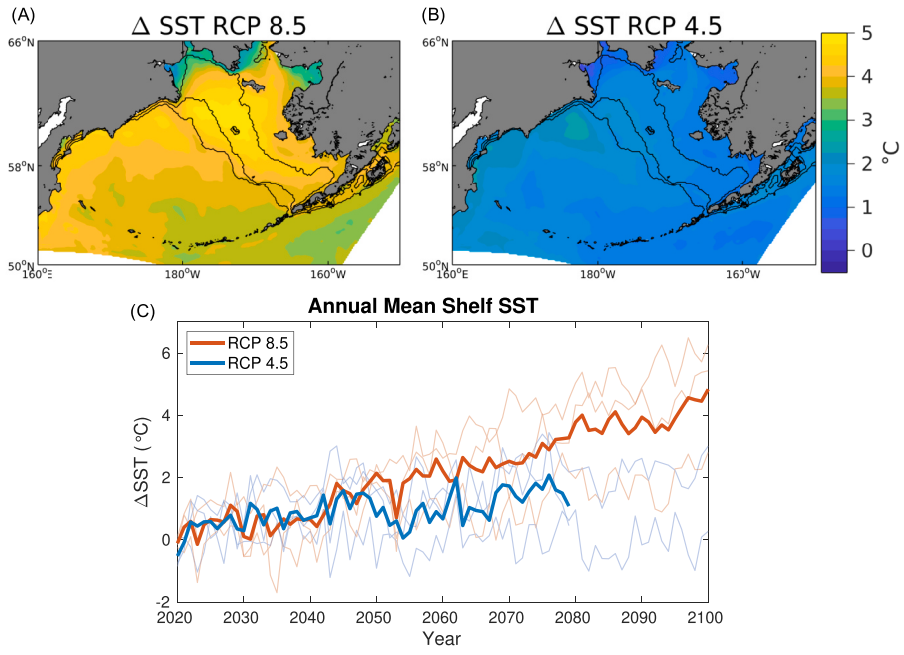

Fig. 2. Ensemble mean change in surface temperature between 2091-2100 and 2011–2020 for (A) RCP 8.5 and (B) RCP 4.5. Contour lines denote the 50, 100, and 200m isobaths. (C) Timeseries of ΔSST for the area-weighted mean shelf. The thick line in (C) represents the ensemble mean, with the thinner lines representing each individual ensemble member. Note that the ensemble mean line for RCP 4.5 ends in 2080 due to the 2080 end date for the B10K-CESM in our ensemble, while the other 2 models continue to 2100. For the spatial plot in RCP 4.5 (B) the end time is 2071–2080 for CESM, and 2091–2100 for the MIROC and GFDL models.

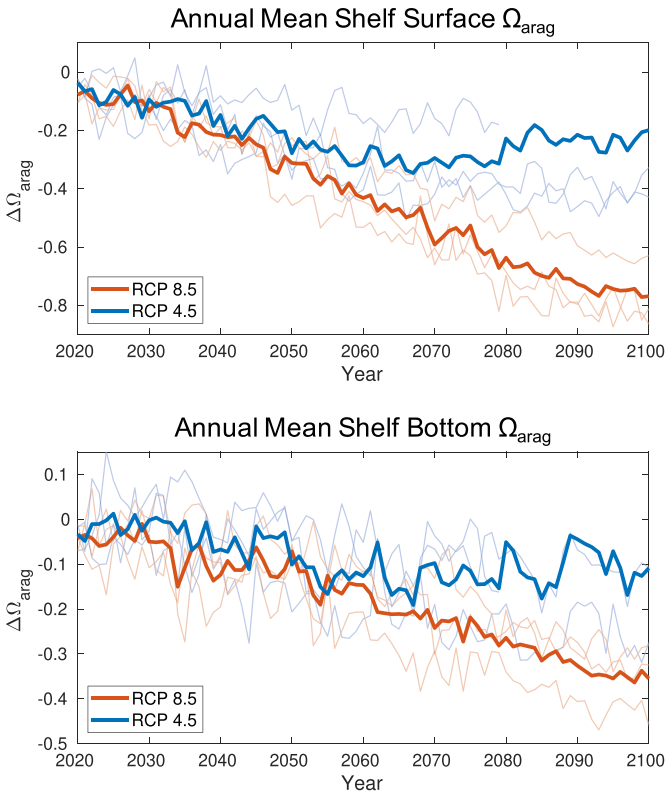

Fig. 3. Timeseries for (top) surface and (bottom) bottom water area-weighted $\Delta\Omega_{arag}$ for the Bering Sea shelf, calculated as the deviation from the 2010–2019 average. The ensemble mean is denoted by the thick line, with the thinner lines representing each individual ensemble member. Note that the B10K-CESM simulation for RCP 4.5 ends in 2080, and the ensemble mean line also ends in 2080 to avoid a sudden change due to switching from 3 ensemble members to 2.

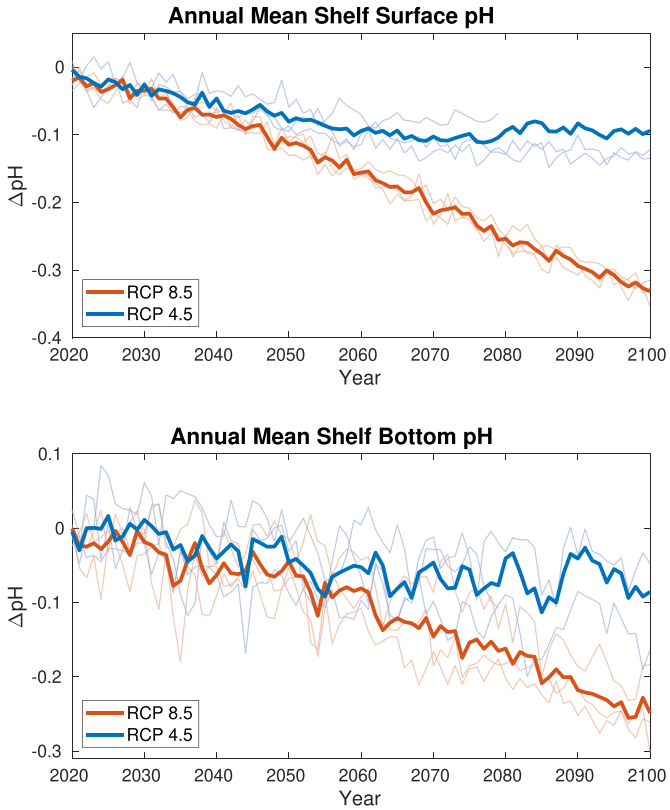

Fig. 4. Same as Fig. 3 but for pH.

models (Hollowed et al., 2020; Holsman et al., 2020; Cheng et al., 2021).

In this study, we utilize a previously developed regional ocean biogeochemical model (Bering10K; Hermann et al., 2013, 2016; Pilcher et al., 2019; Kearney et al., 2020) to dynamically downscale multiple CMIP5 Earth System Models. These model runs are forced using different RCP climate change scenarios to project ocean acidification for the Bering Sea. These projections were produced in tandem with ACLIM

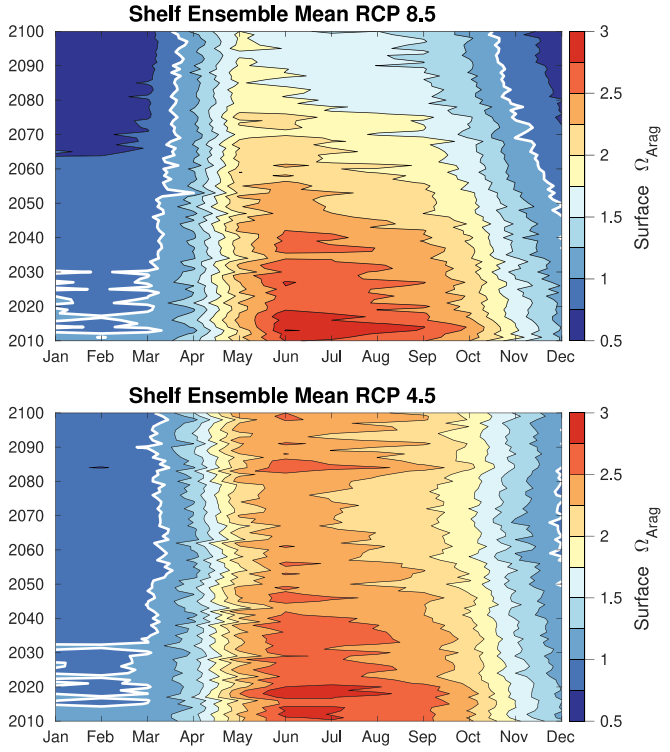

Fig. 5. Ensemble mean surface Ω_{arag} values for the area-weighted shelf (top) RCP 8.5 and (bottom) RCP 4.5 scenarios. The white contour denotes the $\Omega_{arag} = 1$ line.

and follow a similar method to the previous biophysical projections (Hermann et al., 2019). The goal of these OA projections is to provide high spatial-temporal resolution products of changing ocean carbonate chemistry conditions to help inform biological sensitivity experiments and strategic planning for marine fishery management.

2. Methods

2.1. Regional model

The regional model used for the dynamical downscaling is an implementation of the Regional Ocean Modeling System (ROMS; Shchepetkin and McWilliams, 2005; Haidvogel et al., 2008) at 10 km horizontal resolution with 30 terrain-following depth layers (Fig. 1). This model configuration (Bering10K) simulates sea-ice formation and melt and contains tidal mixing. A complete description of the physical model can be found in Hermann et al. (2013) with updates as noted in Kearney et al. (2020). This physical model is coupled to a nutrient-phytoplankton-zooplankton (NPZ) ecosystem model, developed as part of the Bering Sea Ecosystem Study (BESTNPZ; Gibson and Spitz, 2011) and recently updated following Kearney et al. (2020). This ecosystem model contains three nutrients (nitrate, ammonium, and iron), two phytoplankton groups (small and large), five zooplankton groups (microzooplankton, small copepods, large copepods, euphausiids, and jellyfish), and two detrital groups (slow and fast sinking). The model tracks nitrogen through the different ecosystem model groups, which is then converted to carbon when required using a C:N molar ratio of 106:16. The NPZ model also contains an ice biology module with an ice algae, nitrate, and ammonium group, and a benthic sub-model which encompasses a benthic infauna group and a detrital group. The benthic sub-model is based on a simplified version of the European Regional Sea Ecosystem model (ERSEM; Ebenhöh et al., 1995), where benthic infauna graze on pelagic phytoplankton and detritus within 1m of the bottom, and also benthic detritus. Organic material that reaches the bottom is transferred to the benthic detrital pool, with 20% of the material permanently removed due to processes not represented in the model (e.g. burial and off-shelf transport) and an additional 1% removed due to denitrification (Kearney et al., 2020).

Carbonate chemistry is simulated by adding two additional state variables: dissolved inorganic carbon (DIC) and total alkalinity (TA), which are used to calculate the entire carbonate chemistry system following the OCMIP-2 protocols (Orr et al., 1999) and CO2SYS (Lewis et al., 1998). Planktonic respiration and detrital remineralization are the primary DIC sources, while phytoplankton primary production is the primary DIC sink. DIC is also exchanged with the atmosphere according to the gradient in CO_2 partial pressure between the surface ocean and atmosphere (ΔpCO_2) and the wind speed following Wanninkhof (2014). A complete description of the model carbonate chemistry can be found in Pilcher et al. (2019).

A notable addition to the model used here compared to the iteration described in Pilcher et al. (2019) is the incorporation of DIC and TA cycling in waters containing sea ice following the parameterizations of Mortenson et al. (2018). The purpose of the DIC and TA ice parametrizations is to simulate the process of brine rejection and ikaite crystal (a metastable phase of calcium carbonate) precipitation in sea-ice formation. As sea ice forms, dense, high DIC and TA brine is rejected and sinks with the brine rejected salts, leaving relatively lower DIC and TA in the sea ice. When this sea ice melts, the low DIC and TA dilutes the surface waters. Thus, the net effect is downward transport of relatively high DIC and TA waters in regions of ice formation, and a dilution of surface waters with low DIC and TA during ice melt. The formation of ikaite crystals in sea ice occurs following a 2:1 M ratio of TA to DIC (Geilfus et al., 2016; Mortenson et al., 2018). Therefore, sea-ice growth and ikaite formation will increase surface ocean water pCO_2 (due to reducing the TA/DIC ratio of ocean water), while conversely ikaite dissolution during sea ice melt will decrease surface pCO_2 (due to increasing the ocean water TA/DIC ratio).

DIC fluxes associated with ice growth and melt are parameterized as:

$$\varphi_{DIC} = \frac{\partial h_{Ice}}{\partial t} \Delta DIC^{eff} \quad (1)$$

where $\frac{\partial h_{Ice}}{\partial t}$ is the change in sea ice thickness over time and ΔDIC^{eff} represents the effective difference in DIC between sea ice and water and is calculated as:

$$\Delta DIC^{eff} = DIC^{ref}_{SW} - (DIC^{ref}_{ice} + DIC^{ref}_{ikaite}) \quad (2)$$

where DIC^{ref}_{SW} is the reference concentration of DIC in seawater and is set to 2100 mmol C m^{-3}, DIC^{ref}_{ice} is reference concentration of DIC in ice and is set to 400 mmol C m^{-3}, and DIC^{ref}_{ikaite} is the concentration of DIC trapped in ice as ikaite and is set to 50 mmol C m^{-3}. Total alkalinity fluxes associated with ice growth and melt are parametrized according to the following similar equations:

$$\varphi_{TA} = \frac{\partial h_{Ice}}{\partial t} \Delta TA^{eff} \quad (3)$$

$$\Delta TA^{eff} = TA^{ref}_{SW} - (TA^{ref}_{ice} + TA^{ref}_{ikaite}) \quad (4)$$

where TA^{ref}_{SW} is the reference concentration of total alkalinity in seawater and is set to 2200 mmol m^{-3}, TA^{ref}_{ice} is the reference TA of ice and is set to 500 mmol m^{-3}, and TA^{ref}_{ikaite} is the concentration of TA trapped in ice as ikaite and is set to 100 mmol m^{-3}. The values for $DIC^{ref}_{SW}, DIC^{ref}_{ice}, DIC^{ref}_{ikaite}$, $TA^{ref}_{SW}, TA^{ref}_{ice}, TA^{ref}_{ikaite}$ are the same as those chosen by Mortenson et al. (2018) based on limited observational data of these values in Arctic sea ice. These values are kept constant to ensure mass conservation (Mortenson et al., 2018). The reference values for DIC and TA (DIC^{ref}_{SW} and TA^{ref}_{SW}) are reflective of annual mean surface values observed for the

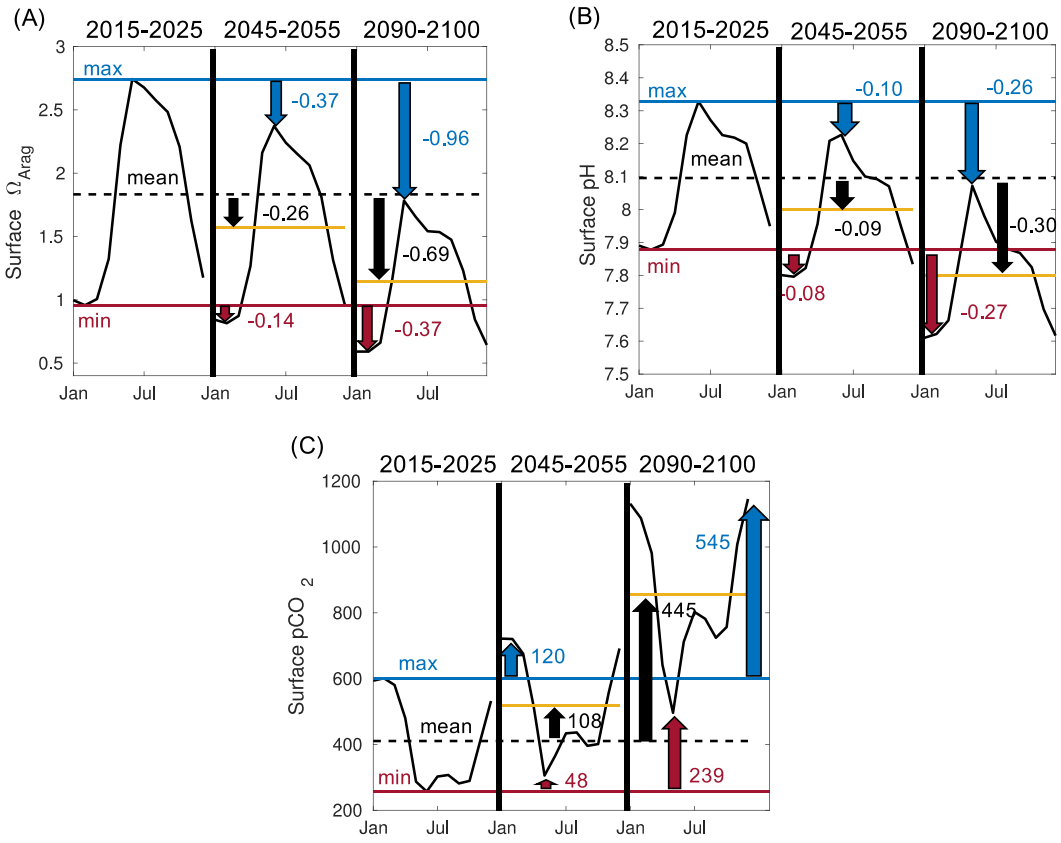

Fig. 6. Seasonal cycle plots for the ensemble mean, area-weighted shelf for (A) Ω_{arag}, (B) pH, and (C) pCO_2 for RCP 8.5. The blue, black, and red lines denote the 2015–2025 seasonal maximum, mean, and minimum values. The corresponding color arrows illustrate the change in these values for the later 2045–2055 and 2090–2100 timeframes. The yellow line denotes the new seasonal mean for the respective timeframe. (For interpretation of the references to color in this figure legend, the reader is referred to the Web version of this article.)

Bering Sea. Implementation of this mechanism did not significantly change model skill metrics for DIC and TA based on comparisons with observational data, though the available data are temporally biased to ice-free summer months when this mechanism is not active.

2.2. CMIP5 models

Following Hermann et al., 2019, we dynamically downscale three CMIP5 models: GFDL-ESM2M (Dunne et al., 2013), MIROC-ESM (Watanabe et al., 2011), and the CESM (Kay et al., 2015). These three models were chosen in part due to their good performance in simulating present conditions the Bering Sea, the accessibility of the required atmospheric forcing variables, and because variability in future projected air temperature over the Bering Sea in these 3 models encompasses ~80% of the variability of the CMIP5 ensemble, with the CESM falling closest to the CMIP5 ensemble mean (Hermann et al., 2019).

The regional downscaling uses atmospheric forcing (air temperature, specific humidity, shortwave and longwave radiation, u and v winds, and precipitation) from the CMIP5 model at daily (MIROC, CESM) or 6 hourly (GFDL) resolution. Output from the CMIP5 model is also used to derive the horizontal boundary conditions for physical variables (u, v velocities, temperature, salinity), and DIC and TA. Nutrient boundary conditions (NO_3 and iron) are kept at present climatological values to limit additional sources of uncertainty that may be generated due to inheriting ESM bias and drift, and to focus on the carbonate chemistry changes driven by surface forcing (i.e. atmospheric CO_2) as opposed to indirect biologically-driven changes from the lateral boundary conditions. The horizontal boundary conditions for the ecological groups (e.g. phytoplankton, zooplankton biomass) are kept at constant, very small seed-population levels (i.e. 1 mmolC m^{-3}). Boundary conditions are at monthly resolution for the physical and nutrient variables and yearly resolution for DIC and TA for GFDL and MIROC (based on output availability), but monthly for CESM. Atmospheric CO_2 follows mean annual values described by the respective Representative Concentration Pathway (RCP; Meinshausen et al., 2011).

Each model run is started in 2006 using initial conditions from a long-term Bering10K hindcast (Pilcher et al., 2019). The model is then continuously run forward in time from 2006 to 2100 using the atmospheric forcing and horizontal boundary conditions from the ESM and RCP scenario. An exception is the CESM RCP 4.5 run which ended in 2080. Weekly-averaged output data were archived from each simulation. We omit the first 4 years of each simulation as model spin-up, and therefore report all results over the 2010–2100 timeframe. Previous work has illustrated that this timeframe is sufficient for the Bering Sea shelf carbonate system to adjust to new input and/or boundary conditions (Pilcher et al., 2019; H. Wang personal communication), largely due to the relatively short residence time of 1–2 years. Each simulation uses the same climatological river runoff forcing, compiled from river gauge data in Alaska and Russia (Kearney, 2019). This river runoff contains seasonally-varying concentrations of DIC and TA following data collected at Pilot Station at the mouth of the Yukon River in Alaska (Striegl et al., 2007; PARTNERS, 2010). While it is likely that the seasonality, magnitude, and biogeochemistry of this runoff will change over the 21st Century due to climate change (Tank et al., 2012; Brown et al., 2019; Terhaar et al., 2019), the exact nature of these changes remains uncertain. Therefore, we use the climatological estimates as a first-order approach.

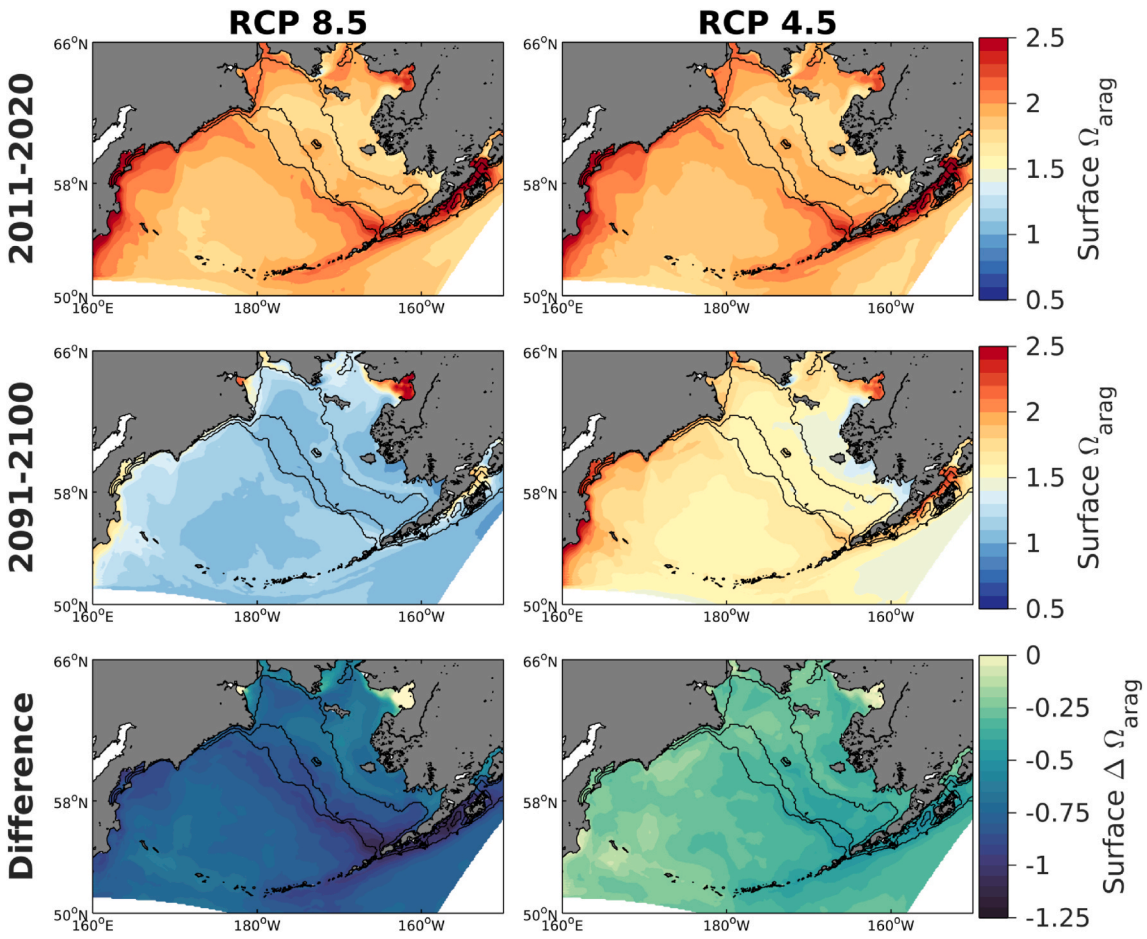

Fig. 7. Spatial plots of ensemble mean surface Ω_{arag} for the 2011–2020 timeframe, the 2091–2100 timeframe, and difference between the two. Left column figures are RCP 8.5 and right are RCP 4.5. The thin black contour lines denote the 50, 100, and 200 m isobaths. Note that the projected end timeframe for B10K-CESM in RCP 4.5 is 2071–2080 (Supplementary Fig. S3).

2.3. Model analysis

All model output is regridded from the native ROMS curvilinear coordinate system (182 × 258 × 30) to a standard latitude-longitude grid at set depth intervals (161 × 251 × 29) using a linear nearest neighbor technique. The depth levels are 5 m thickness each for the upper 20 m, then gradually increase in thickness to a maximum of 250 m for depths below 1000 m. The regridding process has a negligible effect on shelf wide trend values, and is conducted to facilitate analysis and figure visualization. Model values of Ω_{arag} and pH are calculated from model temperature, salinity, DIC, and TA with CO2SYS and the carbonic acid dissociation coefficients of Mehrbach et al. (1973), refit by Dickson and Millero (1987). To distinguish between geochemical changes and the effects of freshwater, we calculate salinity-normalized trends in TA and DIC using the average salinity at each grid cell over 2011–2020, for each respective model simulation. To illustrate spatial changes in model carbonate chemistry variables, we show the difference between a "present" timeframe defined as 2011–2020 and an end of the century timeframe defined as 2091–2100, except for the CESM 4.5 downscaling which uses an end timeframe of 2071–2080 due to the 2080 end date. We elect to use 10-year averages as opposed to a multi-decadal average to avoid diminishing the magnitude of the total change. Our multi-model ensemble approach lessens the impact of interannual climate variability, and indeed the spatial pattern is unchanged when using a 15- or 20-year average. Furthermore, trends in surface carbonate variables are detectable relatively quickly compared to other ocean variables, with previous modeling studies suggesting a time of emergence of 5–15 years for anthropogenic trends in pH and Ω_{arag} (Schlunegger et al., 2019).

3. Results

Dynamically downscaled projections of sea surface temperature illustrate substantial warming throughout the Bering Sea shelf, with notable differences between the two RCP scenarios (Fig. 2). Both scenarios produce similar temperature changes up through 2050, at which point they diverge with the RCP 8.5 scenario nearing an annual mean ΔSST of 2.8–6.3 °C by 2100 compared to 0.3–3.0 °C under RCP 4.5. The MIROC and CESM under RCP 8.5 are distinguishable from the RCP 4.5 simulations, though the colder GFDL RCP 8.5 simulation is not. This warming is spatially heterogenous, with the greatest increase in SST occurring along the middle shelf domain just north of St. Matthew Island under RCP 8.5. The inter-model spread in SST projections closely follows the spread in projected air temperature changes, with the MIROC model warming the most, GFDL model warming the least, and the CESM approximately following the ensemble mean of all three models.

Ensemble mean annual surface (Fig. 3a) and bottom (Fig. 3b) $\Delta\Omega_{arag}$ spatially averaged over the Bering Sea shelf decreases for both RCP scenarios over the 21st Century. This decrease is greater under RCP 8.5 compared to RCP 4.5, and is also greater at the surface compared to the bottom. Annual average Ω_{arag} for the Bering Sea shelf decreases by 0.63–0.86 by the end of the century under RCP 8.5, and by 0.18–0.43 under RCP 4.5. Bottom water Ω_{arag} decrease by 0.28–0.46 for RCP 8.5 and 0.11–0.27 for RCP 4.5. The range in ensemble members is ~0.2 at the surface and 0.1–0.2 at the bottom. Despite this spread, the surface ensemble members are clearly distinguishable between the two RCP

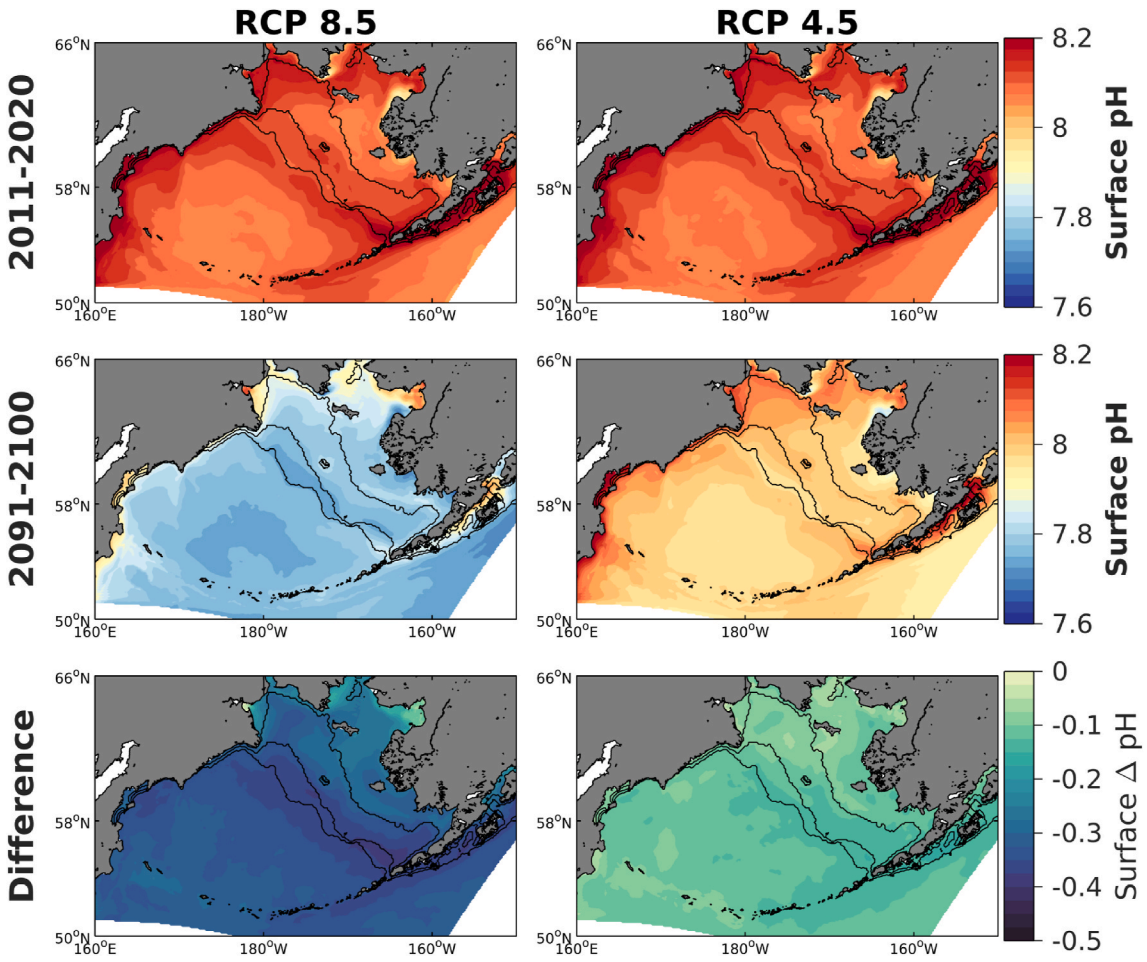

Fig. 8. Same as previous figure, except for surface pH. The thin black contour lines denote the 50, 100, and 200 m isobaths.

scenarios by the end of the century, whereas at the bottom, they still overlap by the end of the century. As with ΔSST, the two scenarios are similar until 2050 when the RCP 4.5 scenario begins to stabilize while the RCP 8.5 values continue to decrease until 2100. Surface and bottom ΔpH (Fig. 4) also decrease under both RCP scenarios, with greater magnitude changes at the surface and under RCP 8.5, similar to the projected changes in $\Delta\Omega_{arag}$. Surface pH decreases by 0.31–0.35 by the end of the century under RCP 8.5, and by 0.07–0.13 under RCP 4.5. The decrease in pH for bottom waters is generally lower but more variable than at the surface, with a decline of 0.18–0.30 for RCP 8.5 and 0.05–0.16 for RCP 4.5. One distinction with ΔpH is that the model spread is smaller compared to the spread in $\Delta\Omega_{arag}$, due in part to the log scale of pH (e.g. the model spread in $[H^+]$ is comparatively greater, as also demonstrated in Fassbender et al. (2021). The model spread in ΔpH (or $[H^+]$) does not overlap between the RCP scenarios at the surface and the bottom by the latter part of the 21st Century.

Model surface Ω_{arag} on the Bering Sea shelf displays a large magnitude seasonal cycle, with relatively low Ω_{arag} values during winter (December–March), followed by much greater values in summer and early fall (June–September, Fig. 5). Surface Ω_{arag} values < 1 begin to regularly occur from January–March between 2015 and 2030 under both RCP scenarios. These water conditions of $\Omega_{arag} < 1$ remain relatively confined to January–March under RCP 4.5, but have a consistently earlier onset in the RCP 8.5 scenario, to the effect that they occur from mid-October to mid-March by the end of the century, comprising 5 months of the year. Furthermore, the degree of winter Ω_{arag} undersaturation deepens under RCP 8.5. Despite these extremely low values by the end of the century, Ω_{arag} consistently rebounds to values above 1 by early April. The timing of this transition from winter undersaturation to summer saturation remains relatively unchanged throughout the entire 21st Century and under both RCP scenarios. Thus, the increase in duration of undersaturated waters in RCP 8.5 is predominately driven by the earlier onset of these conditions.

While the timing of the transition from winter undersaturated to spring-summer supersaturated ($\Omega_{arag} > 1$) conditions remains relatively unchanged in the model projections, the seasonal rebound in summer Ω_{arag} is substantially reduced in RCP 8.5. Fig. 6a illustrates that summer ensemble mean maximum Ω_{arag} values are 0.96 lower by 2100, compared to reductions of 0.69 and 0.37 in the seasonal mean and minimum conditions, respectively. These changes result in a reduced seasonal amplitude and an overall compression of the seasonal cycle. By 2100, summer maximum Ω_{arag} is, on average, slightly lower than the seasonal mean from 2015 to 2025. Furthermore, the seasonal mean by 2100 is approaching the minimum Ω_{arag} values from 2015 to 2025. These seasonal changes are also apparent for surface pH (Fig. 6b), though for pH the seasonal mean by 2100 is lower than the minimum values simulated in 2015–2025. However, these changes to the minimum, maximum, and mean are more uniform for pH than for Ω_{arag}. This results in a pH seasonal amplitude that remains relatively unchanged, compared to the reduced seasonal amplitude for Ω_{arag}. Surface pCO_2 increases substantially by the end of the century, highlighted by a 545 μatm increase in the seasonal max (Fig. 6c). A comparatively smaller increase in the seasonal minimum (239 μatm) results in a nearly doubling of the seasonal amplitude. Overall, the seasonal cycle compresses for Ω_{arag}, expands for pCO_2, and is roughly unchanged for pH.

Spatially, the projected changes in surface Ω_{arag} are heterogenous throughout the Bering Sea shelf, particularly for the RCP 8.5 scenario (Fig. 7). Surface Ω_{arag} decreases by 0.5–0.75 throughout much of the

Table 1
Linear trends from 2010 to 2100 in area-weighted mean shelf surface and bottom variables for the ESM output and the Bering10K downscaled simulations under RCP 8.5 and 4.5 scenarios. Surface values are for the entire shelf, whereas bottom values are divided between the inner (1st row), middle (2nd row), and outer (3rd row) shelf domains. Trend values represent the ensemble mean trend, with the ± signifying the standard deviation.

	ESM 8.5	Bering10K 8.5	ESM 4.5	Bering10K 4.5
Surface Variables				
Temperature (°C yr^{-1})	0.055 ± 0.020	0.053 ± 0.021	0.018 ± 0.014	0.018 ± 0.014
Salinity (mmol m^{-3} yr^{-1})	−0.012 ± 0.007	−0.006 ± 0.002	−0.006 ± 0.003	−0.003 ± 0.002
DIC (mmol m^{-3} yr^{-1})	0.429 ± 0.446	0.809 ± 0.282	0.176 ± 0.230	0.376 ± 0.172
TA (mmol m^{-3} yr^{-1})	−0.770 ± 0.502	−0.398 ± 0.174	−0.372 ± 0.245	−0.140 ± 0.087
sDIC (mmol m^{-3} yr^{-1})	1.24 ± 0.15	1.19 ± 0.24	0.56 ± 0.08	0.57 ± 0.09
sTA (mmol m^{-3} yr^{-1})	0.06 ± 0.08	−0.00 ± 0.22	0.02 ± 0.06	0.06 ± 0.09
pCO_2 (µatm yr^{-1})	6.18 ± 0.33	5.75 ± 0.13	1.91 ± 0.14	1.75 ± 0.09
Ω_{arag} (yr^{-1})	−0.0086 ± 0.0009	−0.0097 ± 0.0015	−0.0043 ± 0.0004	−0.0044 ± 0.0011
pH (yr^{-1})	−0.0045 ± 0.0003	−0.0040 ± 0.0002	−0.0018 ± 0.0001	−0.0015 ± 0.0001
Bottom Variables				
Temperature (°C yr^{-1})	0.053 ± 0.020	0.048 ± 0.021	0.015 ± 0.013	0.013 ± 0.011
	0.053 ± 0.020	0.048 ± 0.016	0.017 ± 0.013	0.012 ± 0.010
	0.037 ± 0.010	0.034 ± 0.009	0.014 ± 0.009	0.011 ± 0.006
Salinity (mmol m^{-3} yr^{-1})	−0.012 ± 0.005	−0.014 ± 0.006	−0.006 ± 0.002	−0.006 ± 0.005
	−0.008 ± 0.003	−0.007 ± 0.002	−0.004 ± 0.002	−0.004 ± 0.002
	−0.001 ± 0.002	−0.003 ± 0.001	−0.001 ± 0.001	−0.002 ± 0.0005
DIC (mmol m^{-3} yr^{-1})	0.29 ± 0.41	0.36 ± 0.27	0.13 ± 0.23	0.23 ± 0.20
	0.57 ± 0.27	0.13 ± 0.40	0.26 ± 0.14	0.12 ± 0.31
	0.82 ± 0.13	0.46 ± 0.23	0.38 ± 0.09	0.24 ± 0.14
TA (mmol m^{-3} yr^{-1})	−0.79 ± 0.36	−0.51 ± 0.18	−0.38 ± 0.20	−0.20 ± 0.12
	−0.48 ± 0.24	−0.45 ± 0.16	−0.25 ± 0.14	−0.17 ± 0.10
	−0.004 ± 0.07	−0.20 ± 0.08	−0.05 ± 0.02	−0.07 ± 0.05
sDIC (mmol m^{-3} yr^{-1})	1.13 ± 0.24	1.33 ± 0.33	0.52 ± 0.13	0.66 ± 0.17
	1.11 ± 0.24	0.61 ± 0.31	0.24 ± 0.11	0.39 ± 0.26
	0.86 ± 0.17	0.68 ± 0.20	0.45 ± 0.10	0.36 ± 0.11
sTA (mmol m^{-3} yr^{-1})	0.06 ± 0.07	0.48 ± 0.35	0.30 ± 0.05	0.24 ± 0.23
	0.06 ± 0.07	0.03 ± 0.07	0.07 ± 0.05	0.09 ± 0.03
	0.04 ± 0.04	0.01 ± 0.05	0.01 ± 0.03	0.05 ± 0.04
pCO_2 (µatm yr^{-1})	7.01 ± 0.50	5.87 ± 0.11	2.21 ± 0.20	2.07 ± 0.28
	8.24 ± 1.31	6.59 ± 1.97	2.85 ± 0.79	2.31 ± 1.98
	6.60 ± 1.48	7.82 ± 0.96	2.63 ± 0.67	2.83 ± 0.31
Ω_{arag} (yr^{-1})	−0.0028 ± 0.0039	−0.0060 ± 0.0007	−0.0015 ± 0.0021	−0.0032 ± 0.0006
	−0.0026 ± 0.0037	−0.0031 ± 0.0011	−0.0014 ± 0.0020	−0.0017 ± 0.0011
	−0.0018 ± 0.0026	−0.0032 ± 0.0010	−0.0013 ± 0.0018	−0.0017 ± 0.0006
pH (yr^{-1})	−0.0043 ± 0.0004	−0.0032 ± 0.0001	−0.0017 ± 0.0001	−0.0013 ± 0.0002
	−0.0042 ± 0.0005	−0.0026 ± 0.0007	−0.0018 ± 0.0002	−0.0011 ± 0.0007
	−0.0032 ± 0.0003	−0.0027 ± 0.0004	−0.0015 ± 0.0002	−0.0012 ± 0.0002

northern Bering Sea and inner shelf domain, while the outer shelf domain and southeastern shelf decrease by 0.75–1.25. The regions of greatest Ω_{arag} decrease occur near the shelf break and the Aleutian Islands near Unimak Pass. Similar spatial patterns are also apparent in RCP 4.5, though the magnitudes are lower. A similar spatial pattern of relatively greater changes on the outer shelf domain is also apparent for surface pH (Fig. 8). These regions of greatest Ω_{arag} and pH decrease also tend to be regions with relatively higher values during the initial 2011–2020 timeframe. Spatial maps for each individual ensemble member are shown in the supplementary material.

Bottom water Ω_{arag} values start the 2011–2020 timeframe already near or below 1 for most of the outer and middle shelf, while the inner shelf remains above 1. Because the inner shelf is very shallow (less than 50 m), most of this region consists of a single mixed layer. Thus, surface and bottom water Ω_{arag} are comparable for the inner shelf. Conversely, middle and outer shelf Ω_{arag} bottom water values are substantially lower than surface waters, particularly in the northwest Bering Sea shelf and the Gulf of Anadyr. By the end of the 21st century under RCP 8.5, bottom water Ω_{arag} has greatly decreased on the Bering Sea shelf, with middle and outer shelf water far below 1 and inner shelf water near 1. This decrease in Ω_{arag} is more muted in the RCP 4.5 scenario, with most of the middle and outer shelf waters experiencing a very slight decrease in Ω_{arag}.

3.1. Comparison to ESM output

Modeled linear trends over the full model timeframe in annually averaged values for waters on the Bering Sea shelf extracted from both the coarse resolution and the downscaled versions of the three ESMs highlight key similarities and differences between the two model resolutions and RCP scenarios (Table 1). Trends in many surface carbonate variables (i.e. sDIC, pCO_2, pH, and Ω_{arag}) are stronger under RCP 8.5 compared to RCP 4.5, and are comparable between the ESMs and the downscaled projections. Increasing temperature and decreasing salinity trends are greater in magnitude under RCP 8.5, though scenario differences are generally not distinguishable from the ensemble uncertainty. Temperature trends at the surface are nearly identical between the downscaled simulations and the default ESM output, with similar magnitudes of ensemble spread. Differences between the trends in DIC and TA compared to the salinity-normalized sDIC and sTA highlight the role of freshening, particularly in the ESMs which display a much greater spread in DIC and TA trends compared to sDIC and sTA, respectively. This is also consistent with stronger decreasing salinity trends in the ESMs compared to the downscaled projections, though the models are not statistically distinguishable. Overall, trends at the bottom are slightly dampened compared to trends at the surface, with comparable magnitudes of ensemble spread, except for bottom Ω_{arag} in the ESMs.

For bottom waters, we further separate trends into the three shelf domains (i.e. inner, middle, outer) to highlight the utility of the higher resolution downscaled simulations. For example, in the downscaled simulations, inner shelf bottom water trends are similar to the respective surface trends due to the shallow depth of the inner shelf. However, this is not always the case for the coarser ESMs, with inner shelf bottom water trends that are significantly different than the surface trends for Ω_{arag} and pH for RCP 8.5. Conversely, bottom water trends under RCP 8.5 on the relatively deeper outer shelf for carbonate variables are often significantly different than the surface in the downscaled simulations (e.g. sDIC, pCO_2, Ω_{arag}, and pH), though this is not true for pCO_2 with the ESMs. Though not statistically distinguishable, the ESMs produce the strongest bottom pCO_2 trend for the middle shelf, while the downscaled projections have the strongest magnitude bottom water trend on the outer shelf. There is also a much greater spread in bottom water Ω_{arag} trends compared to the surface for the ESMs, however the spread between the surface and bottom trends is similar for the downscaled projections.

Although the linear trends in surface carbonate chemistry variables

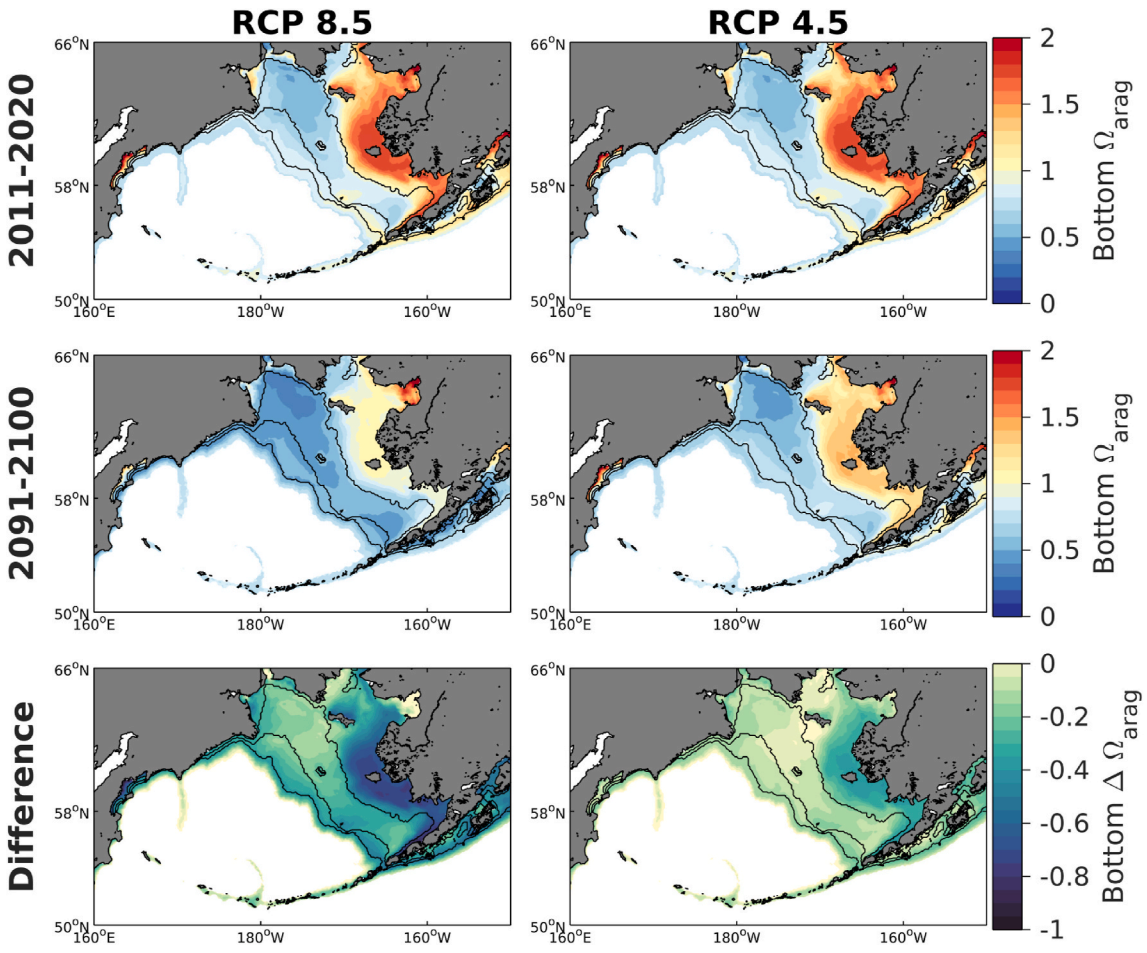

Fig. 9. Same as previous figure except for bottom water Ω_{arag}. The thin black contour lines denote the 50, 100, and 200 m isobaths.

are similar between the ESMs and the downscaled simulations, this is not the case for the actual values due to initial value differences (Figs. 10 and 11). The downscaled simulations generally suggest surface Ω_{arag} values that are greater overall compared to the ESMs (though the coarse MIROC and downscaled CESM are initially nearly identical), particularly for the downscaled MIROC simulation (Fig. 10a). This large difference between the coarse and downscaled MIROC simulations is driven by greater total alkalinity (TA) in the downscaled simulation (Fig. 10c, S1-2). The greater TA values in the Bering10K generate a relatively greater TA/DIC ratio (Fig. S12), which shifts the carbonate system to a comparatively more buffered state, resulting in greater values of Ω_{arag} and pH. Conversely, the higher Ω_{arag} for the downscaled GFDL compared to the coarse version is driven by lower DIC (Fig. 10b). The model spread for Ω_{arag} is substantially greater for the downscaled results compared to the coarse simulations. However, the spread in DIC is greater in the coarse resolutions, while the spread in TA is slightly greater in the downscaled simulations. Overall, the model spread tends to align between the coarse and downscaled simulations (i.e. CESM TA and DIC are the lowest of the three models for both the coarse and downscaled resolutions), though MIROC TA is a notable exception.

Fig. 11 shows the spatial patterns in surface Ω_{arag} under RCP 8.5 between the downscaled simulations and the ESM ensemble mean, regridded to the Bering10K grid. Fig. 11 illustrates greater spatial heterogeneity in the downscaled simulations and overall greater values of Ω_{arag}, which is strongly driven by the B10K-MIROC simulation as illustrated in Fig. 10a. The ESM output depicts a latitudinal pattern of decreasing Ω_{arag} poleward (i.e. towards Bering Strait), which is not readily apparent in the Bering10K results. Rather, Bering10K simulates greater Ω_{arag} in nearshore environments (except for waters located near the Yukon River) and also on the outer Bering Sea shelf and the shelf break. Furthermore, the decrease in Ω_{arag} in Bering10K is strongest along the southeastern Bering Sea shelf and the Aleutian Islands, a pattern that is not produced by the ESMs.

4. Discussion

This study provides the first dynamically downscaled projections of carbonate chemistry variables for the Bering Sea. The downscaled results project substantial changes in surface and bottom water chemistry variables, with greater magnitude changes in the RCP 8.5 scenario compared to RCP 4.5. Annual average Ω_{arag} for the Bering Sea shelf decreases by 0.63–0.86 by the end of the century under RCP 8.5, and by 0.18–0.43 under RCP 4.5. Similarly, surface pH decreases by 0.31–0.35 by the end of the century under RCP 8.5, and by 0.07–0.13 under RCP 4.5. Changes in bottom waters are more muted than at the surface, with a Ω_{arag} decrease of 0.28–0.46 for RCP 8.5 and 0.11–0.27 for RCP 4.5, along with pH declines of 0.18–0.30 for RCP 8.5 and 0.05–0.16 for RCP 4.5. However, bottom waters are already naturally more acidic than surface waters, illustrated by lower overall Ω_{arag} and pH at the start of our model simulations (Figs. 7–9). Thus, annual average bottom water Ω_{arag} for the Bering Sea shelf is near 1 at the start of our model simulations, and is consistently below 1 for all model simulations under RCP 8.5 by the latter half of the 21st Century. In comparison, surface Ω_{arag} remains above 1 throughout the 21st Century for most of our model simulations, though Ω_{arag} does drop below 1 by the end of the century for our GFDL and CESM downscaled runs (Fig. S13). Previous work using output from the global-scale CESM projected annual surface aragonite undersaturation by 2062 for the Bering Sea under RCP 8.5

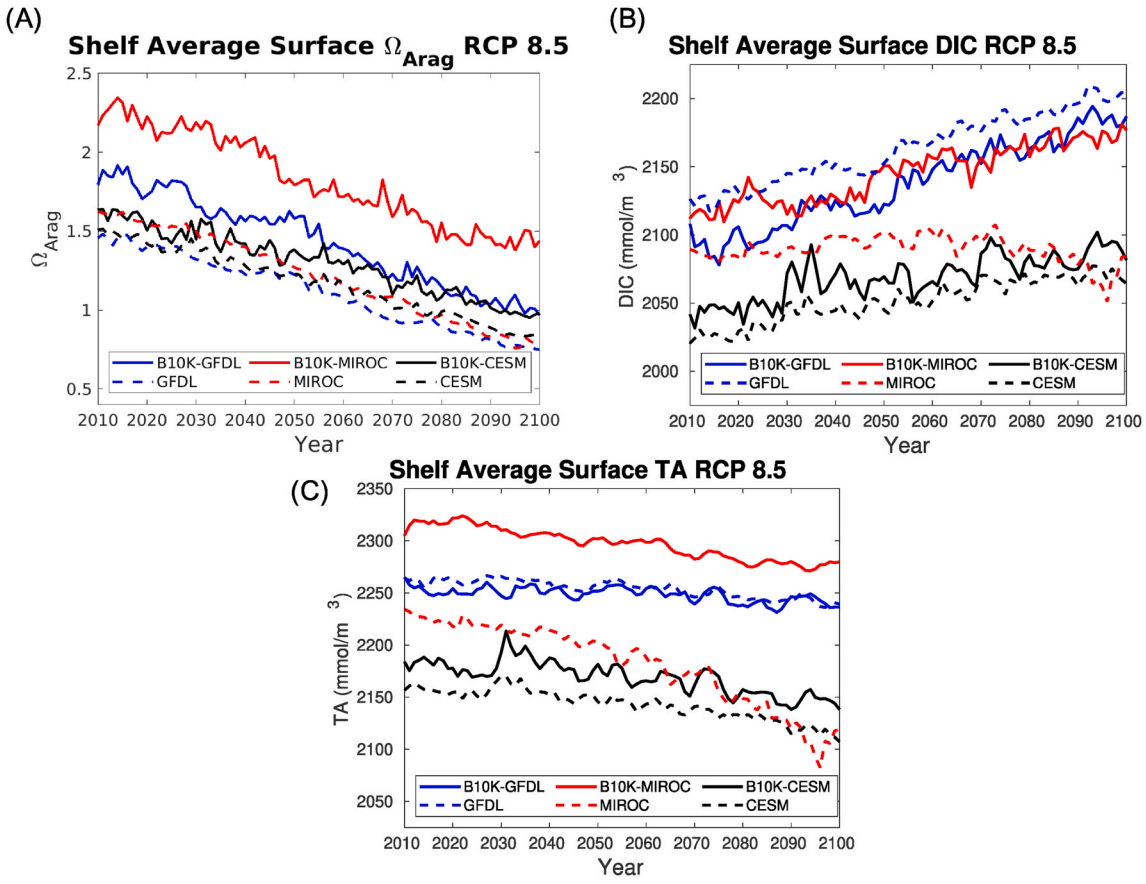

Fig. 10. Timeseries for area-weighted average shelf (A) Ω_{arag}, (B) dissolved inorganic carbon, and (C) total alkalinity for the individual ESM (dashed line) and the respective downscaled simulation (thick line).

(Mathis et al., 2015a). The CESM is the most acidic member of our downscaled model projections, and suggests an earlier (relative to our other two downscaled simulations) timeframe of 2090–2100 for annual $\Omega_{arag} < 1$ under RCP 8.5. These results highlight the importance of utilizing an ensemble of models to quantify uncertainty due to model structural differences.

Although annual surface Ω_{arag} mostly remains above 1 in our downscaled projections, undersaturated conditions do evolve regularly on seasonal timeframes (Fig. 5). In fact, the annual average is not representative of typical water conditions due to the high seasonality in the surface carbonate system. For example, the annual average of ~1.9 in 2010 (Fig. S13) is a transient solution that is passed in May and October during timeframes of rapidly increasing and decreasing Ω_{arag}, respectively (Fig. 5). Instead, the majority of the year is divided into consistently undersaturated conditions in ice-covered winter months, and well-buffered, supersaturated conditions in late spring through early fall associated with phytoplankton productivity (Pilcher et al., 2019). This dynamic continues throughout the entire simulated timeframe, though the summer peak is diminished to a relatively greater extent (Fig. 6). A notable effect of ocean acidification in the RCP 8.5 scenario is the earlier onset and strengthening of winter undersaturated conditions, which does not occur to the same extent in the RCP 4.5 scenario. The increase in undersaturated conditions from approximately 2 months per year in 2010 to 5 months per year in 2100 under RCP 8.5 further underscores the importance of examining seasonal values rather than the annual mean.

Resolving the seasonal changes in carbonate variables is also important for projecting the impacts to marine organisms and ecosystems, which experience the full range of water conditions as opposed to just the annual average. Previous work has highlighted that the seasonal amplitude of carbonate chemistry variables responds differently to increasing ocean carbon uptake and ocean acidification (Sasse et al., 2015; Fassbender et al., 2018; Kwiatkowski and Orr, 2018). This can lead to an increase in the seasonal amplitude of pCO_2 (Gallego et al., 2018), but a decrease for pH and Ω_{arag} (Sasse et al., 2015; Kwiatkowski and Orr, 2018). Our downscaled results also show an increase in the seasonal amplitude of pCO_2 and a decrease in the amplitude of Ω_{arag}, though our simulated pH amplitude did not change. These results indicate that organisms more sensitive to pCO_2 will experience a much greater range in conditions with continued ocean acidification, compared to organisms that are more sensitive to pH or Ω_{arag}.

The projected expansion of relatively more acidic waters can also be conceptualized as a shrinking of the suitable habitat for species that are negatively impacted by decreasing pH or Ω_{arag} (Evans et al., 2019). Fig. 12 illustrates these shrinking optimal habitat conditions at the surface and bottom with regard to particular threshold values of Ω_{arag} and pH for the Bering Sea shelf. The pH threshold values were picked based on previous studies that found negative impacts to red king and tanner crab condition index and survival, particularly for red king crab at pH 7.5 (Long et al., 2013a). Water conditions of pH > 7.8 at the surface occur year-round initially, but begin to erode by 2030 and steadily decrease, composing less than 50% of the year by 2100 under RCP 8.5. Water conditions with pH > 7.5 occur year-round until the latter half of the 21st Century, decreasing to ~60% of the year by 2100. The Long et al. (2013a) experiments observed significant red king crab mortality at pH levels of 7.5, including 100% mortality after 95 days of exposure. The finer spatial resolution of the downscaling also allows for constraining spatial regions of interest, such as the Bristol Bay red king crab fisheries management area (Fig. 13). The patterns are similar to those for the broader shelf, though the erosion of pH > 7.8 conditions

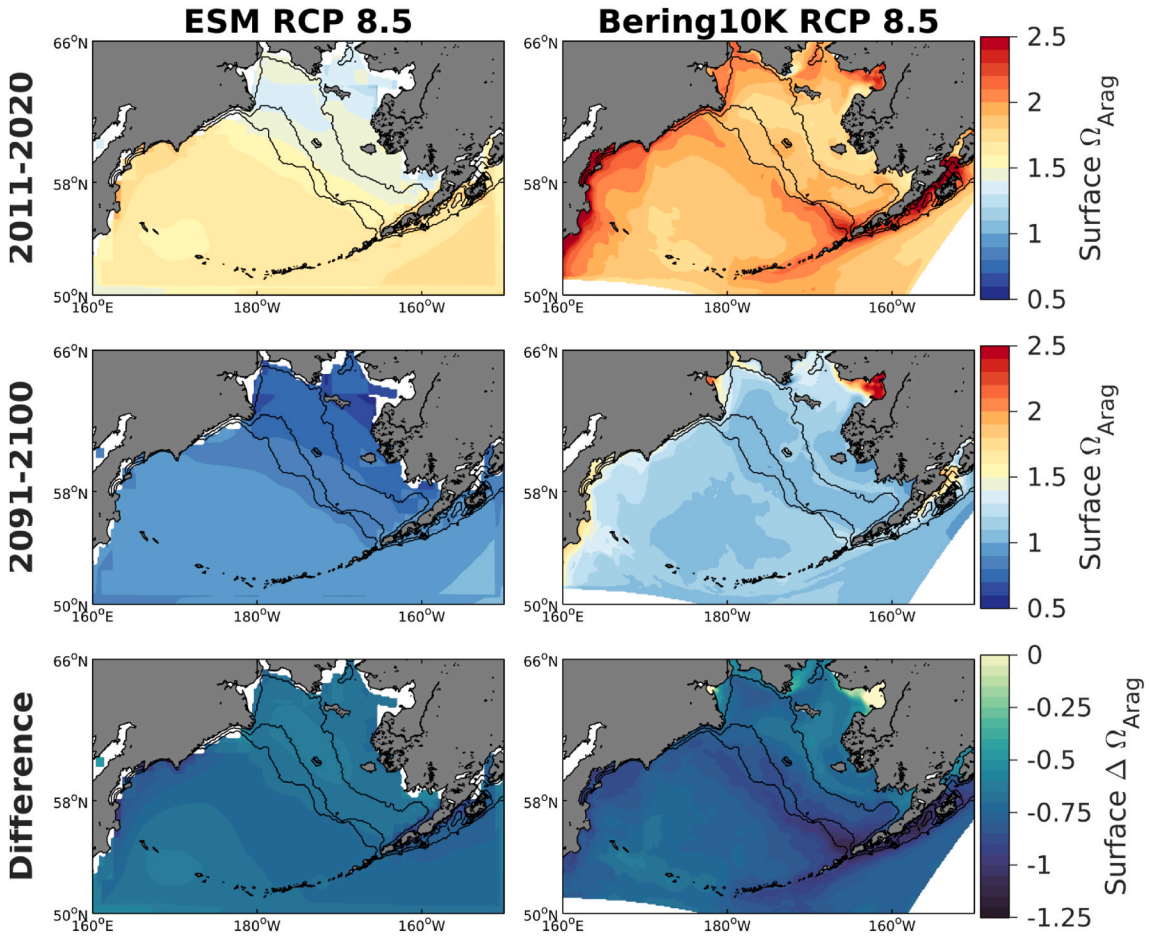

Fig. 11. Same as Figs. 7–9 for surface Ω_{arag} except the left column is now the ESM ensemble average and the right column is the Bering10K downscaled ensemble average.

starts later.

An advantage of the downscaled simulations compared to global-scale ESM output is the capacity to spatially resolve regional hotspots. Our downscaled results identify the outer shelf domain and shelf break, along with the southeastern shelf near the Aleutian Islands and Unimak Pass as OA hotspots. Because these areas are also relatively high in pH and Ω_{arag} during the 2011–2020 timeframe, the greater rate of change diminishes spatial heterogeneity over the shelf. The large changes in the southeastern shelf region are consistent with our previous model hindcast analysis, which also identified this area as a hotspot for changes in carbonate chemistry due to temperature shifts (Pilcher et al., 2019). This region is highly dynamic as it serves as the conduit between the Gulf of Alaska and the Bering Sea, with strong current speeds through Unimak Pass associated with the Alaska Coastal Current (Stabeno et al., 2002). Unimak Pass is relatively narrow (~16 km) and is comprised of only several grid cells in our regional model. It is therefore possible that the spatial resolution is insufficient to fully capture the dynamics, though relatively strong climatological current speeds of 20 cm s^{-1} are simulated with the Bering10K (Hermann et al., 2013), which are slightly faster than the 12.4–17.0 cm s^{-1}observed speeds (Stabeno et al., 2002).

Linear trends in surface temperature, sDIC, sTA, Ω_{arag}, and pH are consistent between the Earth System Model and Bering10K projections for the Bering Sea shelf, with the mean trends often indistinguishable between the two model resolutions considering the model spread (Table 1). A notable exception is surface salinity, with the ESMs projecting a freshening trend two times greater in magnitude (though still statistically indistinguishable) than projected by Bering10K. This difference may be partly attributable to Bering10K maintaining a constant magnitude and seasonality for freshwater river runoff in this suite of simulations, whereas the ESMs generally contain land model components that include changes in the hydrologic cycle. Indeed, freshwater runoff in the Pan-Arctic is projected to increase with warmer temperatures (Rawlins et al., 2010). Thus, while our downscaled projections will incorporate precipitation and evaporation changes from the ESM along with boundary changes in salinity, changes in freshwater runoff are not included. In addition, our projections included a mild (but not negligible) nudging of sea surface salinity to a present-day climatology, which guards against salinity drift, but slightly dampens future changes to the large-scale mean (scaling arguments based on flushing times indicate this should not significantly impact any changes to spatial gradients in salinity which result from changes in ice cover). Bottom water trends are also similar between the ESM and downscaled simulations, though the spread in carbonate variables tends to be lower for the downscaled simulations. This leads to more clearly distinguishable trends in bottom water Ω_{arag} for the different shelf domains in the downscaled simulations, but not for the ESMs.

The similarities between the global ESM and Bering10K mean trends in surface and bottom water variables is noteworthy because previous studies have suggested that downscaling with regional models produces greater magnitude changes in coastal shelf waters (Dussin et al., 2019; Siedlecki et al., 2021). The relatively large spatial extent of the Bering Sea shelf could be one possibility, as this will increase the number of ESM grid cells comprising the shelf, compared to other systems like the California Current. The goal of this comparison is to determine the additional information gained through the computationally expensive process of dynamical downscaling. Comparable trends in carbonate

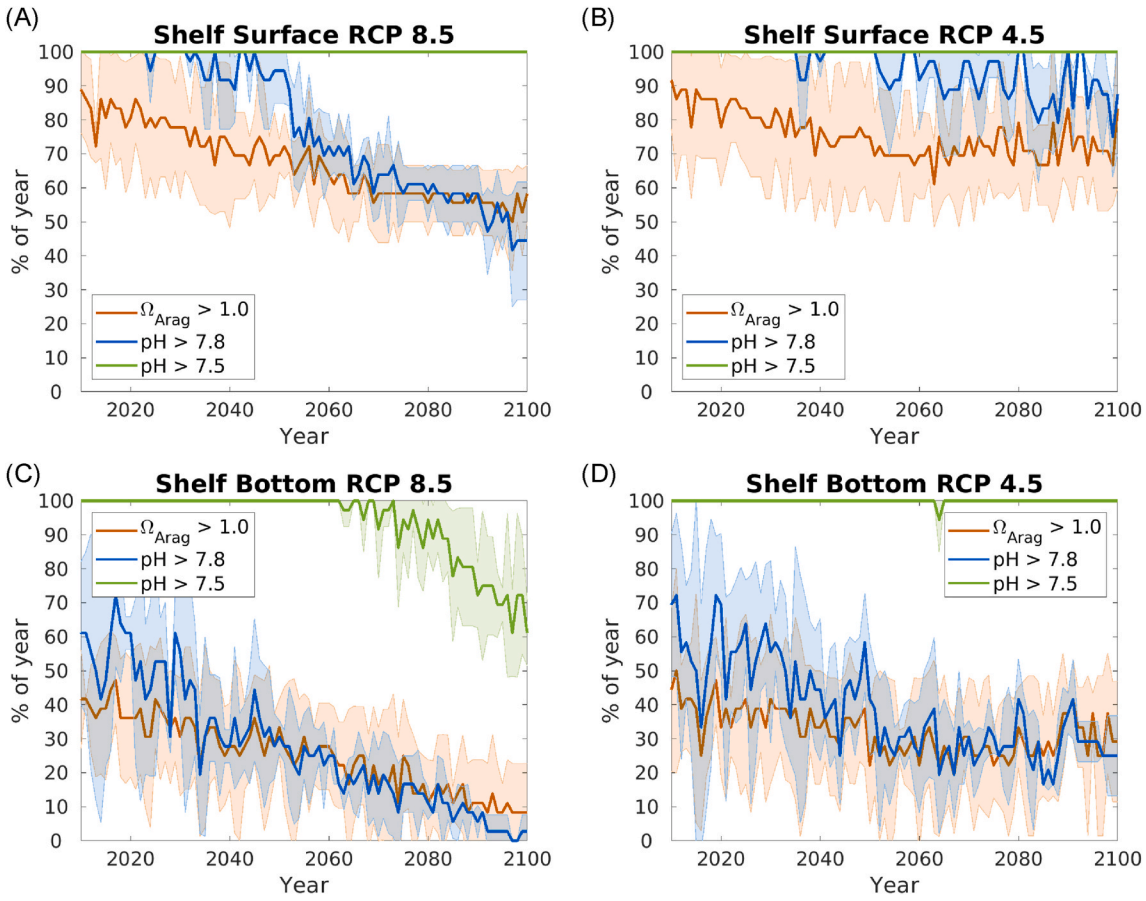

Fig. 12. Percent of the year when waters on the Bering Sea shelf are above the defined threshold values for the surface and bottom under both RCP scenarios.

variables between the ESMs and Bering10K is also somewhat surprising considering significant differences in the TA/DIC ratio, which affects the ocean capacity to absorb atmospheric CO_2 (i.e. the Revelle factor). Furthermore, there are substantial (e.g. > 100 mmol m^{-3}) differences in the TA and DIC concentrations between the ESMs themselves, though the differences tend to co-vary, leading to roughly similar TA/DIC ratios (Fig. S12). However, these results are consistent with previous studies that found the specific emissions scenario is the dominant source of uncertainty for projecting OA rates on multi-decadal timeframes (Rodgers et al., 2015; Frölicher et al., 2016).

The most striking difference between our downscaled results and the ESM output is both the more buffered conditions of our downscaled results and the greater model spread (Fig. 10). Both the magnitude and spatial pattern of Ω_{arag} in the Bering10K compare more favorably to an observed climatology (GLODAPv2; Key et al., 2015; Lauvset et al., 2016) than the ESM output (Fig. S14). Though, we note that the observational data used to generate the climatology for this area are relatively limited. The greater model spread in the Bering10K downscaling compared to the ESMs is unexpected, given that our downscaled results are all using the same physical-biogeochemical model, whereas the ESMs are all using different model components. As previously noted, the DIC and TA model spread is comparable overall between the ESMs and our downscaled results (slightly greater for TA in our downscaled simulations, but slightly less for DIC), yet this spread collapses for Ω_{arag} and pH with the ESMs. The low model spread in the ESMs may be coincidental given the limited 3-member ensemble. These models were selected because they were a good representation of the CMIP5 model spread in atmospheric temperature, but this does not mean they will be similarly representative of the spread in carbonate chemistry. For example, the model spread in surface Ω_{arag} for the Canadian Arctic in the six CMIP5 models utilized by Steiner et al. (2014) is much greater than the spread in our three-member ESM ensemble (~0.4 vs. 0.15 respectively). Nonetheless, a full comparison will require analyzing substantially more CMIP5 models, which is beyond the scope of this manuscript and is left for future work.

The inclusion of the DIC and TA cycling in sea ice was not a substantial driver of changes in carbonate chemistry for our model projections. This is partly because this mechanism has counterbalancing effects on annual timeframes, due to the increase in surface DIC and TA during winter ice formation, but subsequent decrease during spring sea-ice retreat (Fig. S15). Declining seasonal sea ice extent for the Bering Sea with future warming further diminishes the magnitude of this process. Mortenson et al. (2018) also did not find the inclusion of ikaite formation/dissolution to have a substantial impact on annual carbon uptake, however, they noted that the results are sensitive to the concentration of DIC and TA in ikaite due to the 2:1 ratio between TA and DIC. For example, an ikaite composition of 100 mmol m^{-3} TA and 50 mmol m^{-3} DIC generates a 50 mmol m^{-3} disequilibrium, but a composition of 1000 mmol m^{-3} TA and 500 mmol m^{-3} DIC generates a 500 mmol m^{-3} disequilibrium, resulting in a much larger impact on ocean carbon uptake (Mortenson et al., 2018). Further constraining these concentration values will help resolve the relative impact of this mechanism.

As noted earlier, one limitation of our downscaled projections is that freshwater river runoff is kept at a magnitude and seasonality representative of current conditions. With climate change, the magnitude of this runoff is expected to increase (Rawlins et al., 2010). Furthermore, the DIC and TA concentrations of this runoff may also change due to increased mobilization of organic matter from permafrost thawing (Terhaar et al., 2019). These changes will likely impact surface carbonate chemistry on the Bering Sea shelf, particularly in the inner shelf domain. This study also focused exclusively on ocean acidification,

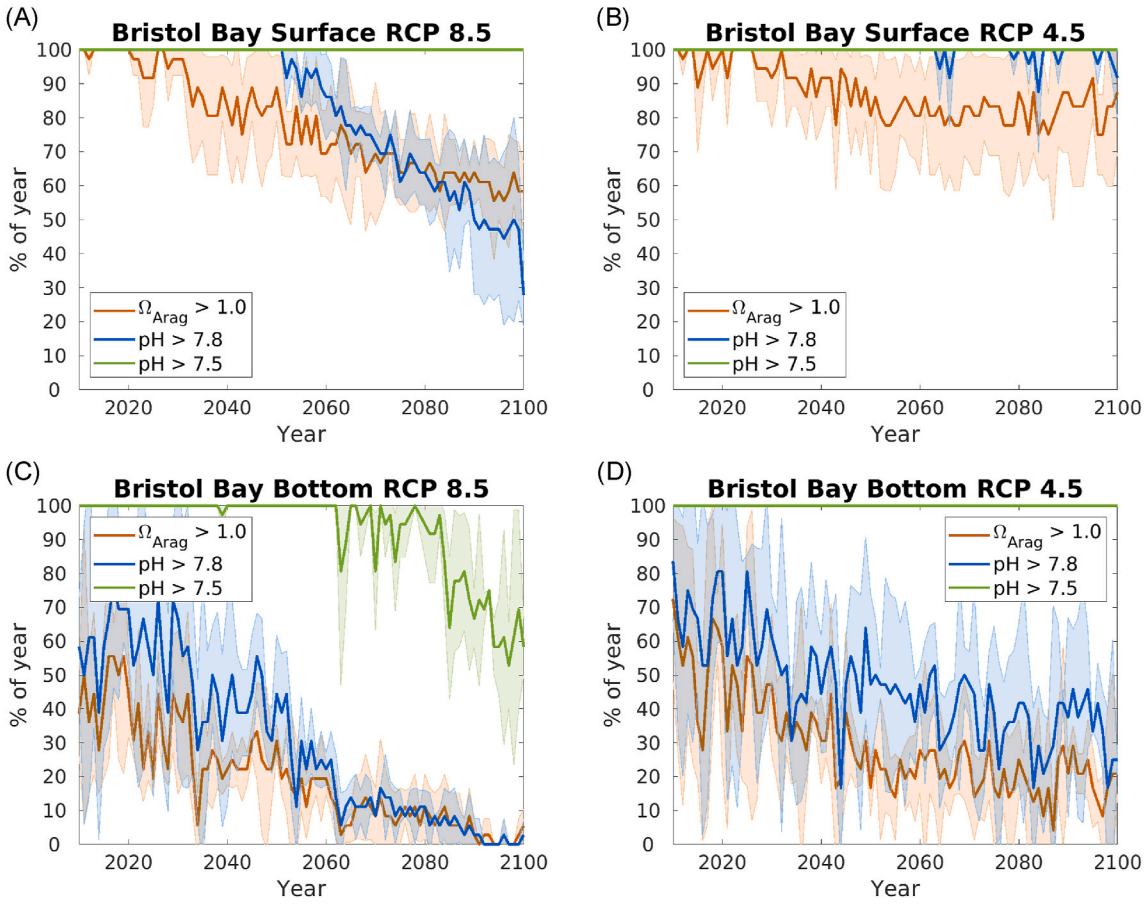

Fig. 13. Same as previous figure except for the Bristol Bay red king crab management region (shown as white box in Fig. 1). (For interpretation of the references to color in this figure legend, the reader is referred to the Web version of this article.)

however, other marine stressors such as rising temperature, deoxygenation, and declining productivity are also projected for the Bering Sea (Bopp et al., 2013; Kwiatkowski et al., 2020). Therefore, incorporating all of these processes is required in order to provide a multi-stressor perspective for future changes to the Bering Sea ecosystem and marine fisheries.

5. Conclusion

Our dynamically downscaled simulations project that Ω_{arag} and pH will steadily decrease over the 21st Century due to continued ocean acidification. Surface Ω_{arag} decreases by 0.63–0.86 under RCP 8.5 and 0.18–0.43 under RCP 4.5, while bottom Ω_{arag} decreases by 0.28–0.46 under RCP 8.5 and 0.11–0.27 under RCP 4.5. Although annual surface Ω_{arag} on the Bering Sea shelf remains above 1 for most of the century under either RCP scenario, undersaturated conditions occur for ~5 months of the year by 2100 under the RCP 8.5 scenario. Seasonally undersaturated conditions also develop under RCP 4.5, but are limited to 2–3 months per year. Spatially, the greatest rates of surface pH and Ω_{arag} decline occur in the southeastern Bering Sea near Unimak Pass, and along the outer shelf domain near the shelf break. Linear trends in surface carbonate variables are comparable between the Earth System Model output and our downscaled simulations. However, bottom water carbonate trends differ for some variables between the two model resolutions, with the higher resolution downscaled model runs more consistently differentiating the Bering Sea shelf domain regions. While the acidification rates are comparable, we find a significant difference between the initial carbonate chemistry system of our downscaled results and the ESMs. The downscaled results depict a more buffered, higher pH and Ω_{arag} system at the start of the 21st Century, compared to the ESM output. This difference is pertinent for determining when water conditions will pass certain Ω_{arag} and pH thresholds experimentally shown to negatively impact marine organisms.

Author statement

Darren Pilcher: Conceptualization, Methodology, Software, Formal analysis, Investigation, Data curation, Writing – Original Draft, Writing – Review & Editing, Visualization, Funding acquisition. **Jessica Cross:** Conceptualization, Methodology, Writing – Review & Editing, Supervision, Project administration. **Albert Hermann:** Conceptualization, Methodology, Software, Data curation, Writing – Review & Editing. **Kelly Kearney:** Conceptualization, Methodology, Software, Data curation, Writing – Review & Editing. **Wei Cheng:** Conceptualization, Methodology, Software, Resources, Data curation, Writing – Review & Editing, Supervision, Project administration. **Jeremy Mathis:** Conceptualization, Resources, Writing – Review & Editing, Supervision, Project administration.

Declaration of competing interest

The authors declare that they have no known competing financial interests or personal relationships that could have appeared to influence the work reported in this paper.

Acknowledgements

This work was facilitated through the use of advanced computational, storage, and networking infrastructure provided by the Hyak supercomputer system at the University of Washington. Stimulating

conversations about the model output were also provided by our colleagues at the UW Cooperative Institute for Climate, Ocean, and Ecosystem Science, and the PMEL Carbon and Eco-FOCI Groups. Funding for this project was provided by the NOAA Arctic Research Program through the Joint Institute for the Study of the Atmosphere and Ocean (JISAO) under NOAA Cooperative Agreement NA15OAR4320063. This is JISAO contribution #2020-1133, PMEL contribution #5234, and Eco-FOCI-1003. We thank the two anonymous reviewers, whose helpful comments greatly improved this manuscript.

Appendix A. Supplementary data

Supplementary data to this article can be found online at https://doi.org/10.1016/j.dsr2.2022.105055.

References

Arrigo, K.R., van Dijken, G.L., 2015. Continued increases in Arctic Ocean primary production. Prog. Oceanogr. 136, 60–70. https://doi.org/10.1016/j.pocean.2015.05.002.

Askren, D.R., 1972. Holocene Stratigraphic Framework—Southern Bering Sea Continental Shelf. M.S. thesis. Univ. of Wash., Seattle, Wash, p. 104.

Bednaršek, N., Naish, K.-A., Feely, R.A., Hauri, C., Kimoto, K., Hermann, A.J., Michel, C., Niemi, A., Pilcher, D., 2021. Integrated assessment of ocean acidification risks to pteropods in the Northern high latitudes: regional comparison of exposure, sensitivity and adaptive capacity. Front. Mar. Sci. 8, 671497. https://doi.org/10.3389/fmars.2021.671497.

Bopp, L., Resplandy, L., Orr, J.C., Doney, S.C., Dunne, J.P., Gehlen, M., et al., 2013. Multiple stressors of ocean ecosystems in the 21st century: projections with CMIP5 models. Biogeosciences 10 (10), 6225–6245. https://doi.org/10.5194/bg-10-6225-2013.

Brown, N.J., Nilsson, J., Pemberton, P., 2019. Arctic Ocean freshwater dynamics: transient response to increasing river runoff and precipitation. J. Geophys. Res. Oceans 124, 5205–5219. https://doi.org/10.1029/2018JC014923.

Cheng, W., Hermann, A.J., Hollowed, A.B., Holsman, K.K., Kearney, K.A., Pilcher, D.J., Stock, C.A., Aydin, K.Y., 2021. Eastern Bering Sea shelf environmental and lower trophic level response to climate forcing: reults of dynamical downscaling from CMIP6. Deep-Sea Res. II. 193, 104975. https://doi.org/10.1016/j.dsr2.2021.104975.

Chierici, M., Fransson, A., 2009. Calcium carbonate saturation in the surface water of the Arctic Ocean: undersaturation in freshwater influenced shelves. Biogeosciences 6, 2421–2431. https://doi.org/10.5194/bg-6-2421-2009.

Coachman, L.K., 1986. Circulation, water masses, and fluxes on the southeastern Bering Sea shelf. Continent. Shelf Res. 5, 23–108. https://doi.org/10.1016/0278-4343(86)90011-7.

Cross, J.N., Mathis, J.T., Bates, N.R., Byrne, R.H., 2013. Conservative and non-conservative variations of total alkalinity on the southeastern Bering Sea shelf. Mar. Chem. 154, 100–112. https://doi.org/10.1016/j.marchem.2013.05.012.

Dickson, A.G., Millero, F.J., 1987. A comparison of the equilibirum constants for the dissociation of carbonic acid in seawater media. Deep Sea Res 34 (10), 1733–1743. https://doi.org/10.1016/0198-0149(87)90021-5.

Doney, S.C., Busch, D.S., Cooley, S.R., Kroeker, K.J., 2020. The impacts of ocean acidification on marine ecosystems and reliant human communities. Annu. Rev. Environ. Resour. 45, 11.1–11.30. https://doi.org/10.1146/annurev-environ-012320-083019.

Drenkard, E.J., et al., 2021. Next-generation regional ocean projections for living marine resource management in a changing climate. ICES (Int. Counc. Explor. Sea) J. Mar. Sci. 1–19. https://doi.org/10.1093/icesjms/fsab100, 0.

Dunne, J.P., John, J.G., Shevliakova, S., Stouffer, R.J., Krasting, J.P., Malyshev, S.L., et al., 2013. GFDL's ESM2 global coupled climate-carbon earth system models. Part II: carbon system formulation and baseline simulation characteristics. J. Clim. 26 (7), 2247–2267. https://doi.org/10.1175/JCLI-D-12-00150.1.

Dussin, R., Curchitser, E.N., Stock, C.A., Van Oostende, N., 2019. Biogeochemical drivers of changing hypoxia in the California Current Ecosystem. Deep-Sea Res. II 169–170 (May), 104590. https://doi.org/10.1016/j.dsr2.2019.05.013.

Ebenhöh, W, Kohlmeier, C, Radford, P.J., 1995. The benthic biological submodel in the European regional seas ecosystem model. Neth. J. Sea Res. 33, 423–452. https://doi.org/10.1016/0077-7579(95)90056-X.

Evans, W., Pocock, K., Hare, A., Weekes, C., Hales, B., Jackson, J., et al., 2019. Marine CO2 patterns in the Northern salish sea. Front. Mar. Sci. 5, 536. https://doi.org/10.3389/fmars.2018.00536.

Fabry, V., McClintock, J., Mathis, J., Grebmeier, J., 2009. Ocean Acidification at high latitudes: the bellwether. Oceanography 22 (4), 160–171. https://doi.org/10.5670/oceanog.2009.105.

Fassbender, A.J., Orr, J.C., Dickson, A.G., 2021. Technical note: interpreting pH changes. Biogeosciences 18, 1407–1415. https://doi.org/10.5194/bg-18-1407-2021.

Fassbender, A.J., Rodgers, K.B., Palevsky, H.I., Sabine, C.L., 2018. Seasonal asymmetry in the evolution of surface ocean pCO_2 and pH thermodynamic drivers and the influence on sea-air CO_2 flux. Global Biogeochem. Cycles 32, 1476–1497. https://doi.org/10.1029/2017GB005855.

Feely, R.A., Sabine, C.L., Lee, K., Berelson, W., Kleypas, J., Fabry, V.J., Millero, F.J., 2004. Impact of anthropogenic CO2 on the CaCO3 system in the oceans. Science 305 (5682), 362–366. https://doi.org/10.1126/science.1097329.

Friedlingstein, P., et al., 2020. Global carbon budget 2020. Earth Syst. Sci. Data 12, 3269–3340. https://doi.org/10.5194/essd-12-3269-2020.

Frölicher, T.L., Rodgers, K.B., Stock, C.A., Cheung, W.W.L., 2016. Sources of uncertainties in 21st century projections of potential ocean ecosystem stressors. Global Biogeochem. Cycles 30 (8), 1224–1243. https://doi.org/10.1002/2015GB005338.

Gallego, M.A., Timmermann, A., Friedrich, T., Zeebe, R.E., 2018. Drivers of future seasonal cycle changes in the oceanic pCO_2. Biogeosciences 15, 5315–5327. https://doi.org/10.5194/bg-15-5315-2018.

Geilfus, N.-X., Galley, R.J., Else, B.G.T., Campbell, K., Papakyriakou, T., Crabeck, O., Lemes, M., Delille, B., Rysgaard, S., 2016. Estimates of ikaite export from sea ice to the underlying seawater in a sea ice-seawater mesocosm. Cryosphere 10 (5), 2173–2189. https://doi.org/10.5194/tc-10-2173-2016.

Gibson, G.A., Spitz, Y.H., 2011. Impacts of biological parameterization, initial conditions, and environmental forcing on parameter sensitivity and uncertainty in a marine ecosystem model for the Bering Sea. J. Mar. Syst. 88 (2), 214–231. https://doi.org/10.1016/j.jmarsys.2011.04.008.

Gruber, N., et al., 2019. The oceanic sink for anthropogenic CO 2 from 1994 to 2007. Science 363 (6432), 1193–1199. https://doi.org/10.1126/science.aau5153.

Haidvogel, D.B., et al., 2008. Ocean forecasting in terrain-following coordinates: formulation and skill assessment of the regional ocean modeling system. J. Comp. Phys. 227 (7), 3595–3624. https://doi.org/10.1016/j.jcp.2007.06.016.

Hermann, A.J., Gibson, G.A., Bond, N.a., Curchitser, E.N., Hedstrom, K., Cheng, W., Wang, M., Stabeno, P.J., Eisner, L., Cieciel, K.D., 2013. A multivariate analysis of observed and modeled biophysical variability on the Bering Sea shelf: Multidecadal hindcasts (1970–2009) and forecasts (2010–2040). Deep Sea Res. II 94, 121–139. https://doi.org/10.1016/j.dsr2.2013.04.007.

Hermann, A.J., Gibson, G.A., Bond, N.A., Curchitser, E.N., Hedstrom, K., Cheng, W., Wang, M., Cokelet, E.D., Stabeno, P.J., Aydin, K., 2016. Projected future biophysical states of the Bering Sea. Deep Sea Res. II 134, 30–47. https://doi.org/10.1016/j.dsr2.2015.11.001.

Hermann, A.J., Gibson, G.A., Cheng, W., Ortiz, I., Aydin, K., Wang, M., Hollowed, A.B., Holsman, K.K., 2019. Projected biophysical conditions of the Bering Sea to 2100 under multiple emission scenarios. ICES J. Mar. Sci. https://doi.org/10.1093/icesjms/fsz043.

Hermann, A.J., Kearney, K., Cheng, W., Pilcher, D., Aydin, K., Holsman, K.K., Hollowed, A.B., 2021. Coupled modes of projected regional change in the Bering Sea from a dynamically downscaling model under CMIP6 forcing. Deep Sea Res. II 194, 104974. https://doi.org/10.1016/j.dsr2.2021.104974.

Holdsworth, A.M., Zhai, L., Lu, Y., Christian, J.R., 2021. Future changes in oceanography and biogeochemistry along the Canadian Pacific continental margin. Front. Mar. Sci. 8, 602991. https://doi.org/10.3389/fmars.2021.602991.

Hollowed, A.B., Holsman, K.K., Haynie, A.C., Hermann, A.J., Punt, A.E., Aydin, K.Y., Ianelli, J.N., Kasperski, S., Cheng, W., Faig, A., Kearney, K.A., Reum, J.C.P., Spencer, P., Spies, I., Stockhausen, W., Szuwalski, C.S., Whitehouse, G.A., Wilderbuer, T.K., 2020. Integrated modeling to evaluate climate change impacts on coupled social-ecological systems in Alaska. Front. Mar. Sci. 6, 775. https://doi.org/10.3389/fmars.2019.00775.

Holsman, K.K., Haynie, A.C., Hollowed, A.B., Reum, J.C.P., Aydin, K., Hermann, A.J., Cheng, W., Faig, A., Ianelli, J.N., Kearney, K.A., Punt, A.E., 2020. Ecosystem-based fisheries management forestalls climate-driven collapse. Nat. Commun. 11, 4579. https://doi.org/10.1038/s41467-020-18300-3.

Hunt, G.L., Stabeno, P., Walters, G., Sinclair, E., Brodeur, R.D., Napp, J.M., Bond, N.A., 2002. Climate change and control of the southeastern Bering Sea pelagic ecosystem. Deep-Sea Res. II 49, 5821–5853. https://doi.org/10.1016/S0967-0645(02)00321-1.

Hunt, G.L., Coyle, K.O., Eisner, L.B., Farley, E.V., Heintz, R.A., Mueter, F., Napp, J.M., Overland, J.E., Ressler, P.H., Salo, S., Stabeno, P.J., 2011. Climate impacts on eastern Bering Sea foodwebs: a synthesis of new data and an assessment of the Oscillating Control Hypothesis. ICES J. Mar. Sci. 68 (6), 1230–1243. https://doi.org/10.1093/icesjms/fsr036.

Hurst, T.P., Fernandez, E.R., Mathis, J.T., 2013. Effects of ocean acidification on hatch size and larval growth of walleye pollock (Theragra chalcogramma). ICES J. Mar. Sci. 70 (4), 812–822. https://doi.org/10.1093/icesjms/fst053.

Hurst, T.P., Copeman, L.A., Haines, S.A., Meredith, S.D., Daniels, K., Hubbard, K.M., 2019. Elevated CO 2 alters behavior, growth, and lipid composition of Pacific cod larvae. Mar. Environ. Res. 145, 52–65. https://doi.org/10.1016/j.marenvres.2019.02.004.

Kay, J.E., Deser, C., Phillips, A., Mai, A., Hannay, C., Strand, G., et al., 2015. The community earth system model (CESM) large ensemble project: a community resource for studying climate change in the presence of internal climate variability. Bull. Am. Meteorol. Soc. 96 (8), 1333–1349. https://doi.org/10.1175/BAMS-D-13-00255.1.

Kearney, K., Hermann, A., Cheng, W., Ortiz, I., Aydin, K., 2020. A coupled pelagic-benthic-sympagic biogeochemical model for the Bering Sea: documentation and validation of the BESTNPZ model (v2019.08.23) within a high-resolution regional ocean model. Geosci. Model Dev. (GMD) 13 (2), 597–650. https://doi.org/10.5194/gmd-13-597-2020.

Kearney, K.A., 2019. Freshwater Input to the Bering Sea , 1950 – 2017, (NMFS-AFSC-388), p. 46.

Key, R.M., Olsen, A., van Heuven, S., Lauvset, S.K., Velo, A., Lin, X., Schirnick, C., Kozyr, A., Tanhua, T., Hoppema, M., Jutterström, S., Steinfeldt, R., Jeansson, E., Ishi, M., Perez, F.F., Suzuki, T., 2015. Global Ocean Data Analysis Project, Version 2 (GLODAPv2), ORNL/CDIAC-162, ND-P093. Carbon Dioxide Information Analysis

Center. Oak Ridge National Laboratory, US Department of Energy, Oak Ridge, Tennessee. https://doi.org/10.3334/CDIAC/OTG.NDP093_GLODAPv2.
Khatiwala, S., Primeau, F., Hall, T., 2009. Reconstruction of the history of anthropogenic CO2 concentrations in the ocean. Nature 462 (7271), 346–349. https://doi.org/10.1038/nature08526.
Kroeker, K.J., Gambi, M.C., Micheli, F., 2013. Community dynamics and ecosystem simplification in a high-CO2 ocean. Proc. Natl. Acad. Sci. Unit. States Am. 110 (31), 12721–12726. https://doi.org/10.1073/pnas.1216464110.
Kwiatkowski, L., Orr, J.C., 2018. Diverging seasonal extremes for ocean acidification during the twenty-first century. Nat. Clim. Change 8 (2), 141–145. https://doi.org/10.1038/s41558-017-0054-0.
Kwiatkowski, L., et al., 2020. Twenty-first century ocean warming, acidification, deoxygenation, and upper-ocean nutrient and primary production decline from CMIP6 model projections. Biogeosciences 17, 3439–3470. https://doi.org/10.5194/bg-17-3439-2020.
Lauvset, S.K., Key, R.M., Olsen, A., van Heuven, S., Velo, A., Lin, X., Schirnick, C., Kozyr, A., Tanhua, T., Hoppema, M., Jutterström, S., Steinfeldt, R., Jeansson, E., Ishii, M., Pérez, F.F., Suzuki, T., Watelet, S., 2016. A new global interior ocean mapped climatology: the 1°x1° GLODAP version 2. Earth Syst. Sci. Data 8, 325–340. https://doi.org/10.5194/essd-8-325-2016.
Lewis, K.M., van Dijken, G.L., Arrigo, K.R., 2020. Changes in phytoplankton concentration now drive increased Arctic Ocean primary production. Science 369, 198–202. https://doi.org/10.1126/science.aay8380.
Lewis, E.R., Wallace, D.W.R., 1998. Program developed for CO2 system calculations. Rep. BNL-61827. Oak Ridger, TN: U.S. Dep. of Energy, Oak Ridge Natl. Lab., carbon dioxide. Inf. Anal. Cent.
Long, W.C., Swiney, K.M., Foy, R.J., 2016. Effects of high pCO2 on Tanner crab reproduction and early life history, Part II: carryover effects on larvae from oogenesis and embryogenesis are stronger than direct effects. ICES J. Mar. Sci. 73 (3), 836–848. https://doi.org/10.1093/icesjms/fsv251.
Long, W.C., Swiney, K.M., Harris, C., Page, H.N., Foy, R.J., 2013a. Effects of ocean acidification on Juvenile Red king crab (Paralithodes camtschaticus) and tanner crab (Chionoecetes bairdi) growth, condition, calcification, and survival. PLoS One 8 (4), e60959. https://doi.org/10.1371/journal.pone.0060959.
Long, W.C., Swiney, K.M., Foy, R.J., 2013b. Effects of ocean acidification on the embryos and larvae of red king crab, *Paralithodes camtschaticus*. Mar. Pollut. Bull. 69, 38–47. https://doi.org/10.1016/j.marpolbul.2013.01.011.
Mathis, J., Cross, J., Evans, W., Doney, S., 2015a. Ocean Acidification in the surface waters of the Pacific-Arctic boundary regions. Oceanography 25 (2), 122–135. https://doi.org/10.5670/oceanog.2015.36.
Mathis, J.T., Cooley, S.R., Lucey, N., Colt, S., Ekstrom, J., Hurst, T., Hauri, C., Evans, W., Cross, J.N., Feely, R.A., 2015b. Ocean acidification risk assessment for Alaska's fishery sector. Prog. Oceanogr. 136, 71–91. https://doi.org/10.1016/j.pocean.2014.07.001.
Mathis, J.T., Cross, J.N., Bates, N.R., 2011. Coupling primary production and terrestrial runoff to ocean acidification and carbonate mineral suppression in the eastern Bering Sea. J. Geophys. Res. 116 (C2), C02030. https://doi.org/10.1029/2010JC006453.
McKinley, G.A., Fay, A.R., Lovenduski, N.S., Pilcher, D.J., 2017. Natural variability and anthropogenic trends in the ocean carbon sink. Ann. Rev. Mar. Sci 9 (1), 125–150. https://doi.org/10.1146/annurev-marine-010816-060529.
Mehrbach, C., Culberson, C.H., Hawley, J.E., Pytkowicx, R.M., 1973. Measurement of the apparent dissociation constants of carbonic acid in seawater at atmospheric pressure. Limnol. Oceanogr. 18 (6), 897–907.
Meinshausen, M., et al., 2011. The RCP greenhouse gas concentrations and their extensions from 1765 to 2300. Climatic Change 109 (1), 213–241. https://doi.org/10.1007/s10584-011-0156-z.
Moore, S.E., Stabeno, P.J., 2015. Synthesis of Arctic Research (SOAR) in marine ecosystems of the Pacific Arctic. Prog. Oceanogr. 136, 1–11. https://doi.org/10.1016/j.pocean.2015.05.017.
Mortenson, E., Steiner, N., Monahan, A.H., Miller, L.A., Geilfus, N.-X., Brown, K., 2018. A model-based analysis of physical and biogeochemical controls on carbon exchange in the upper water column, sea ice, and atmosphere in a seasonally ice-covered Arctic strait. J. Geophys. Res., Oceans 123 (10), 7529–7549. https://doi.org/10.1029/2018JC014376.
Orr, J.C., Najjar, R., Sabine, C.L., Joos, F., 1999. Abiotic-HOWTO. Internal OCMIP report. https://www.cgd.ucar.edu/oce/OCMIP/HOWTO-Abiotic.pdf, 25.
Orr, J.C., et al., 2005. Anthropogenic ocean acidification over the twenty-first century and its impact on calcifying organisms. Nature 437 (7059), 681–686. https://doi.org/10.1038/nature04095.
Pan-Arctic River Transport of Nutrients, Organic Matter, and Suspended Sediments Project [PARTNERS], 2010. Arctic river biogeochemistry data set. Available at: http://ecosystems.mbl.edu/partners/.
Pilcher, D.J., Naiman, D.M., Cross, J.N., Hermann, A.J., Siedlecki, S.A., Gibson, G.A., Mathis, J.T., 2019. Modeled effect of coastal biogeochemical processes, climate variability, and ocean acidification on aragonite saturation state in the Bering Sea. Front. Mar. Sci. 5, 508. https://doi.org/10.3389/fmars.2018.00508.
Punt, A.E., Foy, R.J., Dalton, M.G., Long, W.C., Swiney, K.M., 2016. Effects of long-term exposure to ocean acidification conditions on future southern Tanner crab (Chionoecetes bairdi) fisheries management. ICES J. Mar. Sci. 73 (3), 849–864. https://doi.org/10.1093/icesjms/fsv205.
Rawlins, M.A., et al., 2010. Analysis of the Arctic system for freshwater cycle intensification: observations and expectations. J. Clim. 23 (21), 5715–5737. https://doi.org/10.1175/2010JCLI3421.1.
Rodgers, K.B., Lin, J., Frölicher, T.L., 2015. Emergence of multiple ocean ecosystem drivers in a large ensemble suite with an Earth system model. Biogeosciences 12 (11), 3301–3320. https://doi.org/10.5194/bg-12-3301-2015.
Sasse, T.P., McNeil, B.I., Matear, R.J., Lenton, A., 2015. Quantifying the influence of CO_2 seasonality on future ocean acidification. Biogeosciences 12 (8), 5907–5940. https://doi.org/10.5194/bgd-12-5907-2015.
Schlunegger, S., Rodgers, K.B., Sarmiento, J.L., Frölicher, T.L., Dunne, J.P., Ishii, M., Slater, R., 2019. Emergence of anthropogenic signals in the ocean carbon cycle. Nat. Clim. Change 9 (9), 719–725. https://doi.org/10.1038/s41558-019-0553-2.
Semiletov, I., Pipko, I., Gustafsson, Ö., Anderson, L.G., Sergienko, V., Pugach, S., Dudarev, O., Charkin, A., Gukov, A., Bröder, L., Andersson, A., Spivak, E., Shakhova, N., 2016. Acidification of East Siberian Arctic Shelf waters through addition of freshwater and terrestrial carbon. Nat. Geosci. 9, 361–365. https://doi.org/10.1038/ngeo2695.
Seung, C.K., Dalton, M.G., Punt, A.E., Poljak, D., Foy, R., 2015. Economic impacts of changes in an Alaska crab fishery from ocean acidification. Clim. Change Econ. 1550017. https://doi.org/10.1142/S2010007815500177, 06(04).
Shchepetkin, A.F., McWilliams, J.C., 2005. The regional oceanic modeling system (ROMS): a split-explicit, free-surface, topography-following-coordinate oceanic model. Ocean Model. 9 (4), 347–404. https://doi.org/10.1016/j.ocemod.2004.08.002.
Siedlecki, S.A., Pilcher, D.J., Howard, E.M., Deutsch, C., MacCready, P.M., Norton, E.L., Frenzel, H., Newton, J., Feely, R.A., Alin, S.R., Klinger, T., 2021. Coastal processes modify projections of some climate-driven stressors in the California Current System. Biogeosciences 18, 2871–2890. https://doi.org/10.5194/bg-2020-279.
Stabeno, P.J., Schumacher, J.D., Ohtani, K., 1999. The physical oceanography of the Bering Sea. In: Loughlin, T.R., Ohtani, K. (Eds.), Dynamics Ofthe Bering Sea: A Summary of Physical, Chemical, and Biological Characteristics, and a Synopsis of Research on the Bering Sea. Alaska Sea Grant, Fairbanks, Alaska.
Stabeno, P.J., Reed, R.K., Napp, J.M., 2002. Transport through Unimak Pass, Alaska. Deep-Sea Res. II 49 (26), 5919–5930. https://doi.org/10.1016/S0967-0645(02)00326-0.
Stabeno, P.J., Bell, S.W., 2019. Extreme conditions in the Bering Sea (2017–2018): record-breaking low sea-ice extent. Geophys. Res. Lett. 46 https://doi.org/10.1029/2019GL083816.
Steiner, N.S., Christian, J.R., Six, K.D., Yamamoto, A., Yamamoto-Kawai, M., 2014. Future ocean acidification in the Canada Basin and surrounding Arctic Ocean from CMIP5 earth system models. J. Geophys. Res. Oceans 119 (1), 332–347. https://doi.org/10.1002/2013JC009069.
Striegl, R.G., Dornblaser, M.M., Aiken, G.R., Wickland, K.P., Raymond, P.A., 2007. Carbon export and cycling by the Yukon, Tanana, and Porcupine rivers, Alaska, 2001-2005. Water Resour. Res. 43 (2), 2001–2005. https://doi.org/10.1029/2006WR005201.
Tank, E.E., Frey, K.E., Striegl, R.G., Raymond, P.A., Holmes, R.M., McClelland, J.W., Peterson, B.J., 2012. Landscape-level controls on dissolved carbon flux from diverse catchments of the circumboreal. Global Biogeochem. Cycles 26, GB4018. https://doi.org/10.1029/2011GB004192.
Terhaar, J., Orr, J.C., Ethé, C., Regnier, P., Bopp, L., 2019. Simulated Arctic Ocean response to doubling of riverine carbon and nutrient delivery. Global Biogeochem. Cycles 33, GB006200. https://doi.org/10.1029/2019GB006200, 2019.
Terhaar, J., Torres, O., Bourgeois, T., Kwiatkowski, L., 2021a. Arctic Ocean acidification over the 21st century co-driven by anthropogenic carbon increases and freshening in the CMIP6 model ensemble. Biogeosciences 18, 2221–2240. https://doi.org/10.5194/bg-18-2221-2021.
Terhaar, J., Lauerwald, R., Regnier, P., Gruber, N., Bopp, L., 2021b. Around one third of current Arctic Ocean primary production sustained by rivers and coastal erosion. Nat. Commun. 12, 169. https://doi.org/10.1038/s41467-020-20470-z.
Vancoppenolle, M., Bopp, L., Madec, G., Dunne, J., Ilyina, T., Halloran, P.R., Steiner, N., 2013. Future Arctic Ocean primary productivity from CMIP5 simulations: uncertain outcome, but consistent mechanisms. Global Biogeochem. Cycles 27, 605–619. https://doi.org/10.1002/gbc.20055.
Vonk, J.E., Sánchez-García, L., van Dongen, B.E., Alling, V., Kosmach, D., Charkin, A., Semiletov, I.P., Dudarev, O.V., Shakhova, N., Roos, P., Eglington, T.I., Andersson, A., Gustafsson, Ö., 2012. Activation of old carbon by eriosion of coastal and subsea permafrost in Arctic Siberia. Nature 489, 137–140. https://doi.org/10.1038/nature11392.
Wanninkhof, R., 2014. Relationship between wind speed and gas exchange over the ocean revisited. Limnol Oceanogr. Methods 12, 351–362. https://doi.org/10.4319/lom.2014.12.351.
Ward, N.D., et al., 2020. Representing the function and sensitivity of coastal interfaces in Earth system models. Nat. Commun. 11, 2458. https://doi.org/10.1038/s41467-020-16236-2.
Watanabe, S., et al., 2011. MIROC-ESM 2010: model description and basic results of CMIP5-20c3m experiments. Geosci. Model Dev. (GMD) 4 (4), 845–872. https://doi.org/10.5194/gmd-4-845-2011.
Wiese, F.K., Wiseman, W.J., Van Pelt, T.I., 2012. Bering Sea linkages. Deep Sea Res. II 65–70, 2–5. https://doi.org/10.1016/j.dsr2.2012.03.001.